

1 **The large-scale, long-term coupling of temperature, hydrology, and water**
2 **isotopes**

3 Nicholas Siler*

4 *College of Earth, Ocean, and Atmospheric Sciences, Oregon State University, Corvallis, Oregon*

5 Adriana Bailey

6 *National Center for Atmospheric Research, Boulder, Colorado*

7 Gerard H. Roe

8 *Department of Earth and Space Sciences, University of Washington, Seattle, Washington*

9 Christo Buizert

10 *College of Earth, Ocean, and Atmospheric Sciences, Oregon State University, Corvallis, Oregon*

11 Bradley Markle

12 *Department of Geological Sciences, University of Colorado, Boulder, Colorado*

13 David Noone

14 *Department of Physics, University of Auckland, Auckland, New Zealand*

15 *Corresponding author: Nicholas Siler, nick.siler@oregonstate.edu

ABSTRACT

16 The stable isotope ratios of oxygen and hydrogen in polar ice cores are known to record environ-
17 mental change, and they have been widely used as a paleothermometer. Although it is known to be
18 a simplification, the relationship is often explained by invoking a single condensation pathway with
19 progressive distillation to the temperature at the location of the ice core. In reality, the physical
20 factors are complicated, and recent studies have identified robust aspects of the hydrologic cycle's
21 response to climate change that could influence the isotope-temperature relationship. In this study,
22 we introduce a new zonal-mean isotope model derived from radiative transfer theory, and incorpo-
23 rate it into a recently developed moist energy balance climate model (MEBM), thus providing an
24 internally consistent representation of the tight physical coupling between temperature, hydrology,
25 and isotope ratios in the zonal-mean climate. The isotope model reproduces the observed pattern of
26 meteoric $\delta^{18}\text{O}$ in the modern climate, and allows us to evaluate the relative importance of different
27 processes for the temporal correlation between $\delta^{18}\text{O}$ and temperature at high latitudes. We find
28 that the positive temporal correlation in polar ice cores is predominantly a result of suppressed
29 high-latitude evaporation with cooling, rather than local temperature changes. The same mecha-
30 nism also explains the difference in the strength of the isotope-temperature relationship between
31 Greenland and Antarctica.

32 **1. Introduction**

33 The proportions of different isotopes in atmospheric water reflect the full set of hydrologic
34 processes that add, remove, transport, and mix the gaseous, liquid, and solid constituents of that
35 water. Because many of these processes are temperature-dependent, the isotopic composition of
36 water that precipitates to the surface reflects the combined hydrologic and temperature history
37 of the vapor from which it condenses. Geologic repositories of precipitation isotope ratios,
38 such as speleothems and polar ice cores, thus provide a crucial source of information about past
39 hydroclimate states.

40 The physical controls on isotopic fractionation have long been studied as a branch of chemistry
41 (e.g., Urey 1947), and that understanding has been used to infer the environmental conditions
42 reflected in the isotope ratios of atmospheric water, and especially precipitation (e.g., Dansgaard
43 1964). Because water vapor is often transported thousands of kilometers along complex trajectories
44 (Trenberth 1998), precipitation that falls at any one location reflects the aggregated histories of
45 vapor parcels that have evaporated from vastly different regions (Johnsen et al. 1989; Sodemann
46 and Stohl 2009; Singh et al. 2016a). For this reason, the isotope ratios in precipitation are an
47 inherently integrative measure of the global hydroclimate. This is both a strength and a weakness.
48 It is a strength because the isotopic composition of precipitation at a single location can be assumed
49 to reflect large-scale information about the atmospheric state. But it is also a weakness because the
50 full set of processes that the water vapor experienced on all of the trajectories that ultimately led
51 to precipitation at one location greatly complicates the interpretation of those records.

52 Given this physical complexity, it is perhaps surprising that robust statistical relationships are
53 widely observed between precipitation isotope ratios and local climate variables (e.g., Galewsky
54 et al. 2016). Most notably, in the middle and high latitudes, the $\delta^{18}\text{O}$ and $\delta^2\text{H}$ of precipitation are

55 strongly correlated with local surface temperature (e.g., Dansgaard 1964; Jouzel et al. 1997). This
56 so-called “temperature effect” is often interpreted as a result of Rayleigh distillation, operating
57 within a simple model of the extratropical hydrologic cycle that consists of a continuous stream
58 of water vapor that evaporates from the subtropical oceans and progressively condenses as it
59 moves poleward to cooler temperatures. Assuming constant Rayleigh fractionation and a source
60 temperature of 20 °C, Dansgaard (1964) showed that this model implies a spatial regression slope
61 between precipitation $\delta^{18}\text{O}$ (δ_p) and surface temperature of around 0.7 ‰ K⁻¹, which closely
62 matches the relationship found in observations. If one further assumes that the source temperature
63 is relatively constant in time, the same result can also be applied to the temporal regression slope,
64 allowing historical temperatures to be reconstructed from δ_p variations recorded in polar ice cores
65 (Grootes et al. 1993; Jouzel et al. 1997; Johnsen et al. 2001; Jouzel et al. 2003; Masson-Delmotte
66 et al. 2006). However, independent temperature reconstructions from boreholes (Johnsen et al.
67 1995; Cuffey et al. 1994, 1995; Dahl-Jensen et al. 1998) and nitrogen isotopes (Severinghaus et al.
68 1998; Buizert et al. 2014; Kindler et al. 2014) suggest that the temporal regression slope between
69 temperature and δ_p at a given site can differ substantially from the observed spatial slope, with
70 values ranging from less than 0.4 ‰ K⁻¹ in Greenland to more than 1 ‰ K⁻¹ in Antarctica (e.g.,
71 Buizert et al. 2021). This difference between spatial and temporal slopes should not be surprising
72 given that δ_p is known to be sensitive to multiple environmental factors besides local temperature,
73 such as changes in the seasonality of precipitation (Krinner et al. 1997; Werner et al. 2000), shifting
74 atmospheric circulation patterns (Charles et al. 1994; Rhines and Huybers 2014), and changes in the
75 temperature and spatial distribution of evaporation source regions (Boyle 1997; Masson-Delmotte
76 2005; Werner et al. 2001; Sodemann et al. 2008; Lee et al. 2008). Indeed, given this complexity,
77 the bigger surprise may be that δ_p is correlated with local temperature at all. Such correlations

78 seem to indicate an underlying coherence to the hydroclimate system, whereby a change in one
79 variable necessarily implies synchronous changes in all the others.

80 In recent years, research into anthropogenic warming has led to substantial progress in under-
81 standing the hydrologic cycle and its role in the global climate system. In the global mean, the
82 latent heat of evaporation and condensation must be balanced by other terms in the energy bud-
83 gets of the surface and atmosphere (Boer 1993; Allen and Ingram 2002). This, combined with
84 thermodynamic constraints on the partitioning between latent and sensible heat fluxes from the
85 surface (e.g., Siler et al. 2019), acts as a strong constraint on evaporation (and hence precipitation,
86 since water must be conserved). As a result, GCM simulations tend to show a relatively modest
87 increase in global-mean precipitation of 2-3 % per Kelvin of global-mean warming—substantially
88 less than the $\sim 7\% \text{ K}^{-1}$ increase in atmospheric water vapor expected from the Clausius–Clapeyron
89 equation (e.g., Allen and Ingram 2002; Held and Soden 2006). If the basic structure and inten-
90 sity of the atmospheric circulation remains similar, the mean-state patterns of moisture transport
91 and convergence will increase with warming at a similar rate as water vapor, implying a wetter
92 deep-tropics, a drier subtropics, and a wetter middle-and-high latitudes (Held and Soden 2006).
93 Furthermore, because vapor and vapor transport increase at a larger rate globally than precipitation
94 or evaporation, simple scaling arguments imply that water vapor will also travel farther and reside
95 longer in the atmosphere, on average, as the climate warms (Trenberth 1998; Singh et al. 2016b).

96 Recent studies have further demonstrated that the spatial patterns of temperature and hydrologic
97 change are tightly coupled through their joint dependency on meridional atmospheric heat transport,
98 of which latent heat (and hence hydrology) is a key component. In particular, Siler et al. (2018)
99 showed that the spatial patterns of zonal-mean temperature and hydrology in the current climate—
100 as well as the spatial patterns of temperature and hydrologic change predicted within an ensemble of
101 GCMs—can be accurately emulated using a simple one-dimensional (1D) energy balance model,

102 in which poleward energy transport is represented as the linear diffusion of near-surface moist
103 static energy (i.e., sensible plus latent heat).

104 This energetic framework provides a self-consistent understanding of the coupling between
105 zonal-mean hydrology and surface temperature, both in the modern climate and in the context of
106 climate changes. In this paper, we add to this framework a simple representation of Lagrangian
107 vapor transport and Rayleigh fractionation. We show that the fractionation of isotopes due to
108 evaporation, meridional transport, and precipitation can be represented mathematically by the
109 equations of radiative transfer. Using this framework, we can reproduce the observed meridional
110 distribution of δ_p in the modern climate, suggesting the observed patterns are the result of a few
111 simple principles.

112 We also investigate the cause of the observed positive temporal regression slope between δ_p and
113 temperature at high latitudes. We find that predicted changes in temperature and vapor transport
114 distance would, by themselves, cause the temporal slope to be negative. We conclude that the
115 positive slope found in the ice core record primarily reflects the sensitive dependence of evaporation
116 on the mean-state climate, and hence a redistribution of evaporation patterns with climate change,
117 which is a predictable consequence of thermodynamic constraints on the partitioning of surface
118 energy fluxes.

119 **2. Meridional vapor transport: a 1D Lagrangian perspective**

120 Any representation of Rayleigh fractionation requires a method of tracking, in a Lagrangian
121 sense, the movement of water vapor from its source (where it evaporates) to its sink (where it
122 precipitates). Here we present a simple Lagrangian model of meridional vapor transport, which
123 derives from the essential similarity between the depletion of vapor transport by precipitation and
124 the attenuation of radiation through scattering or absorption.

125 In radiative transfer, when a beam of light propagates through a scattering or absorbing medium,
 126 the intensity I of the beam progressively decreases. The fractional decrease in I per distance of
 127 propagation is defined as the attenuation coefficient μ :

$$\mu(x) \equiv -\frac{1}{I} \frac{dI}{dx}. \quad (1)$$

128 As the beam propagates between two points, x_1 and x_2 , it experiences a cumulative attenuation of

$$\tau(x_1, x_2) = \int_{x_1}^{x_2} \mu(x) dx, \quad (2)$$

129 which is defined as the optical depth of the layer. The decrease in intensity across the layer is given
 130 by Beer's law,

$$\frac{I(x_2)}{I(x_1)} = f(x_1, x_2), \quad (3)$$

131 where

$$f(x_1, x_2) = e^{-\tau(x_1, x_2)} \quad (4)$$

132 represents the transmittance of the layer.

133 We can apply these same equations to the zonal-mean hydrologic cycle, where the depletion of
 134 vapor transport by precipitation is similar to the attenuation of light by absorption and scattering.
 135 In this analogy, the attenuation coefficient (Eq. 1) represents the fraction of vapor that condenses
 136 per distance x of meridional transport. In the time average, this is given by

$$\mu(x) \approx 2\pi a^2 \frac{P(x)}{|F(x)|}, \quad (5)$$

137 where x is the sine of latitude, a is earth's radius, P is the zonal-mean precipitation rate at the
 138 surface (in units of latent heat flux, Wm^{-2}), and F is the zonally-integrated net northward latent
 139 heat transport (in W). Because F must vanish at the poles, and the meridional divergence of F is
 140 proportional to the zonal-mean evaporation E minus P , we can write

$$F(x) = 2\pi a^2 \int_{-1}^x E(\tilde{x}) - P(\tilde{x}) d\tilde{x}. \quad (6)$$

141 Thus, $\mu(x)$ depends only on the zonal-mean patterns of E and P . We can then use Eqs. 2 and
 142 4 to define hydrologic analogs to $\tau(x_1, x_2)$ and $f(x_1, x_2)$, with the latter representing the fraction
 143 of vapor that evaporates at a particular source latitude x_1 and reaches a downstream latitude x_2
 144 without precipitating. To be physically realistic, we set $f(x_1, x_2) = 0$ for all x_2 that are not directly
 145 downstream from x_1 , as determined by the sign of F .

146 The above framework allows us to characterize meridional vapor transport from both a source
 147 and sink perspective. First, from the source perspective, we define $w_e(x_1, x_2)$ as the distribution of
 148 precipitation across all x_2 that results from evaporation at a single source latitude x_1 . Expressed
 149 as a probability density function (PDF), this distribution is equal to the absolute value of $\partial f / \partial x_2$,
 150 which simplifies to

$$w_e(x_1, x_2) = \mu(x_2) f(x_1, x_2). \quad (7)$$

151 Second, from the sink perspective, we define $w_p(x_1, x_2)$ as the meridional distribution of evapo-
 152 ration that results in precipitation at a particular sink latitude. As noted by Fisher (1990), this is
 153 proportional to $f(x_1, x_2)$, weighted by the magnitude of evaporation at the source:

$$w_p(x_1, x_2) = \frac{f(x_1, x_2) E(x_1)}{\int_{-1}^1 f(x_1, x_2) E(x_1) dx_1}. \quad (8)$$

154 The difference between these two perspectives is illustrated in the second row of Fig. 1, which
 155 shows examples of w_e (Fig. 1c) and w_p (Fig. 1d) at representative source and sink latitudes of
 156 $\sin^{-1} x_1 = \pm 40^\circ$ and $\sin^{-1} x_2 = \pm 80^\circ$, respectively, computed using annual-mean values of $E(x)$ and
 157 $P(x)$ from ERA5 reanalysis (Fig. 1a,b; Hersbach et al. 2020). The w_e PDFs (Fig. 1c) are almost
 158 mirror images of each other, decaying roughly exponentially from each source latitude toward its
 159 respective pole. By comparison, the PDFs of w_p (Fig. 1d) exhibit more spatial structure and less
 160 symmetry, with a narrower distribution and sharper local peak in the Northern Hemisphere (red)
 161 than in the Southern Hemisphere (blue). This asymmetry is not caused by differences in the spatial

162 pattern of $f(x_1, x_2)$, which is similar between the hemispheres. Rather, it stems from $E(x)$, which
 163 is greater at high latitudes in the Northern Hemisphere than in the Southern Hemisphere (Fig. 1a,
 164 red line), thereby giving more weight to northern high-latitude sources in Eq. 8.

165 From the PDFs of w_e and w_p , we can also calculate the average distance that vapor travels
 166 from and to a given latitude. The meridional distance traveled by a single vapor molecule over
 167 its lifetime is equal to $a|\theta_2 - \theta_1|$, where $\theta_1 = \sin^{-1}x_1$ and $\theta_2 = \sin^{-1}x_2$ are the source and sink
 168 latitudes, respectively (in radians). Therefore, the average meridional transport distance of *all*
 169 vapor originating at x_1 , defined here as $\overline{d_e}(x_1)$, is equal to the average of $a|\theta_2 - \theta_1|$ over all sink
 170 latitudes, weighted by w_e :

$$\overline{d_e}(x_1) = \int_{-1}^1 a|\theta_2 - \theta_1|w_e(x_1, x_2)dx_2. \quad (9)$$

171 Because the attenuation coefficient μ tends to exhibit little variability over small spatial scales, we
 172 show in Appendix A1 that Eq. 9 can be approximated as

$$\overline{d_e}(x_1) \approx \frac{a}{\cos \theta_1} \mu(x_1)^{-1}. \quad (10)$$

173 Therefore, just as in radiative transfer (e.g., Wallace and Hobbs 2006), μ can be interpreted as an
 174 inverse length scale of vapor transport, with large values implying that vapor travels a short distance
 175 before precipitating. Conversely, from a sink perspective, vapor that *precipitates* at a particular
 176 latitude will have travelled an average distance of

$$\overline{d_p}(x_2) = \int_{-1}^1 a|\theta_2 - \theta_1|w_p(x_1, x_2)dx_1. \quad (11)$$

177 Equations 9 and 11 represent two distinct ways of defining the average vapor transport distance.
 178 Whereas $\overline{d_e}$ measures how far vapor travels *from* a particular *source* latitude, $\overline{d_p}$ measures how far
 179 vapor travels *to* a particular *sink* latitude. The results of these contrasting perspectives are shown in
 180 the bottom row of Fig. 1, along with the approximate form of $\overline{d_e}$ given by Eq. 10 (Fig. 1e, dashed

181 lines). These were computed using annual-mean values of $E(x)$ and $P(x)$, so they underestimate
 182 the true transport distance in much of the tropics, where the direction of F changes with the
 183 seasons. Poleward of $\sim 20^\circ$, however, the impact of seasonal variability is small (Supplemental
 184 Fig. 1). At these latitudes, the two definitions of transport distance diverge sharply. From the
 185 source perspective (Fig. 1e), $\overline{d_e}$ is approximately symmetric between the Northern and Southern
 186 Hemispheres, reaching a maximum of around 1000 km near 40° and decreasing roughly linearly
 187 to zero at the poles. This behavior is captured well by the approximation in Eq. 10 (dashed line),
 188 demonstrating that $\overline{d_e}$ mostly reflects an increase in μ with latitude. From the sink perspective,
 189 however, transport distance ($\overline{d_p}$) generally increases with latitude outside the tropics (Fig. 1f),
 190 implying that precipitation at high latitudes originates from farther away than precipitation at
 191 lower latitudes. The spatial pattern of $\overline{d_p}$ is also highly asymmetric at high latitudes, with much
 192 larger values in the Southern Hemisphere than in the Northern Hemisphere. Like the hemispheric
 193 differences in w_p discussed previously (Fig. 1d), this asymmetry in $\overline{d_p}$ stems from asymmetry
 194 in E , which causes a larger fraction of high-latitude precipitation in the Southern Hemisphere
 195 to originate from remote sources. This asymmetry will prove to be crucial to understanding the
 196 hemispheric differences in δ_p at high latitudes.

197 3. Isotope Model

198 Just as $\overline{d_p}$ represents the weighted-average transport distance of all upstream sources (Eq. 11),
 199 the average value of δ_p at a particular latitude is given by

$$\overline{\delta_p}(x_2) = \int_{-1}^1 \delta_p(x_1, x_2) w_p(x_1, x_2) dx_1, \quad (12)$$

200 where $\delta_p(x_1, x_2)$ is the δ of precipitation at x_2 that results from evaporation at x_1 . By definition,
 201 this is related to the isotope ratio R_p by

$$\delta_p(x_1, x_2) = \left(\frac{R_p(x_1, x_2)}{R_{std}} - 1 \right) \times 1000, \quad (13)$$

202 where R_{std} is the isotope ratio of Vienna Standard Mean Ocean Water (VSMOW), and the factor
 203 of 1000 reflects the conversion to permil (‰).

204 To find $\overline{\delta_p}(x_2)$, let us first consider a single vapor parcel that evaporates at x_1 with an initial
 205 isotope ratio of $R_e(x_1)$, and then progressively condenses as it is transported to the north or south.
 206 Along the way, the isotope ratio of the vapor (R_v) evolves according to

$$\frac{D \ln R_v}{Dx} = (\alpha - 1) \frac{D \ln q}{Dx}, \quad (14)$$

207 where α is the effective fractionation factor and $D \ln q / Dx$ is the fractional change in the parcel's
 208 specific humidity with latitude, which is equal and opposite to the fractional condensation rate
 209 (note that D/Dx represents the material derivative following the parcel). Equilibrium values of α
 210 vary from 1.009 at 30° to 1.025 at -50°C (Majoube 1970, 1971), but at temperatures below -20°C
 211 the increase with cooling is mostly offset by non-equilibrium kinetic effects (see Appendix A2 and
 212 Supplemental Fig. 2). We account for these dependencies later, but for now let us assume that α
 213 is constant, and equal to the global average effective fractionation. This allows us to integrate Eq.
 214 14 directly, yielding

$$R_v(x_1, x_2) \approx R_e(x_1) f(x_1, x_2)^{\alpha-1}, \quad (15)$$

215 where $f(x_1, x_2)$ is the hydrologic transmittance (Eq. 4). Equation 15 is equivalent to Rayleigh
 216 distillation along a meridional pathway. Assuming that the isotopic content of condensed water is
 217 conserved as it falls to the surface, the isotope ratio of precipitation is then given by

$$R_p(x_1, x_2) = \alpha R_v(x_1, x_2). \quad (16)$$

218 Now suppose that evaporation and condensation exhibit roughly the same fractionation, such that
 219 $\alpha \approx R_{std}/R_e$. Applying the first-order Taylor approximation, $f^{\alpha-1} \approx 1 + (\alpha - 1) \ln(f)$, Eqs. 12-16
 220 combine to give

$$\overline{\delta_p}(x_2) \approx -\epsilon \overline{\tau}(x_2), \quad (17)$$

221 where ϵ is defined in the conventional way,

$$\epsilon \equiv (\alpha - 1) \times 1000, \quad (18)$$

222 and

$$\overline{\tau}(x_2) = \int_{-1}^1 \tau(x_1, x_2) w_p(x_1, x_2) dx_1. \quad (19)$$

223 Thus, the average value of δ_p at a given latitude scales approximately linearly with $\overline{\tau}$, which
 224 represents the average path-integrated attenuation experienced by all vapor present at that latitude.

225 To test how well Eq. 17 captures the distribution of $\overline{\delta_p}$ of ^{18}O in the modern climate, we
 226 compute $\overline{\tau}(x_2)$ using observed zonal-mean values of $E(x)$ and $P(x)$ from ERA5 reanalysis, and
 227 set $\epsilon = 10 \text{ ‰}$ everywhere, following Bailey et al. (2018). Fig. 2a-c shows the resulting meridional
 228 profiles of $\overline{\delta_p}$ (dashed red line) during Boreal summer (July-August), Boreal winter (December-
 229 February), and the annual mean, computed using average profiles of E and P from each time period.
 230 Blue circles represent observed values of δ_p from rain gauges and—in the annual mean—Antarctic
 231 snow. At all latitudes and across the annual cycle, the predicted values of $\overline{\delta_p}$ capture much of the
 232 observed meridional pattern (blue line). In the tropics, seasonal variations in $\overline{\delta_p}$ coincide with the
 233 migration of the intertropical convergence zone into the summer hemisphere, indicating a negative
 234 correlation with precipitation that is consistent with the so-called “amount effect” (Dansgaard
 235 1964). The model also captures most of the hemispheric asymmetry in $\overline{\delta_p}$ in the annual mean (Fig.
 236 2c), correctly predicting more negative values at high latitudes in the Southern Hemisphere than in

237 the Northern Hemisphere. Because $\tau(x_1, x_2)$ generally increases with transport distance $|\theta_2 - \theta_1|$,
238 this asymmetry is closely tied to the hemispheric differences in $\overline{\delta_p}$ discussed in Section 2.

239 Our approximation of $\overline{\delta_p}$ can be made somewhat more realistic by accounting for spatial vari-
240 ability in α and R_e . To do this, we approximate α as a function of surface temperature (T_s) using
241 the empirical equations of Majoube (1970, 1971), and adjust for kinetic effects at sub-freezing
242 temperatures (see Appendix A2). For $R_e(x)$, we use the Craig-Gordon model (Craig and Gordon
243 1965), which takes into account non-equilibrium kinetic effects, as well as the temperature and
244 isotope ratio of the near-surface atmosphere (see Appendix A3).

245 The solid red lines in Fig. 2a-c show the resulting profiles of $\overline{\delta_p}$ when these approximations for
246 α and R_e are incorporated in Eq. 12. Compared with the simpler approximation in Eq. 17 (dashed
247 red line), the full solution exhibits less depletion of ^{18}O at low latitudes, reflecting less fractionation
248 during evaporation when using the more sophisticated Craig-Gordon model (Supplemental Fig.
249 3). At high latitudes, this difference is mostly offset by greater fractionation during condensation
250 at cold temperatures (Majoube 1970, 1971, Supplemental Fig. 2), resulting in better agreement
251 between the two $\overline{\delta_p}$ profiles.

252 While the full solution agrees somewhat better with observations at most latitudes, the two
253 solutions are quite similar overall, supporting the conclusion of Bailey et al. (2018) that most of
254 the observed spatial and temporal variability in $\overline{\delta_p}$ can be explained by the spatial patterns of E
255 and P . In the next section, we apply this result to better understand the response of $\overline{\delta_p}$ to climate
256 change.

4. The isotopic response to Last Glacial Maximum climate change

The preceding analysis shows that the spatial pattern of the climatology of $\overline{\delta_p}$ depends on $E(x)$, $P(x)$, and $T_s(x)$. We therefore anticipate that the sensitivity of $\overline{\delta_p}$ to climate change will depend on the full spatial structure of temperature and hydrologic change, and not just on local temperature.

We now consider three idealized scenarios to isolate the impact of different aspects of hydroclimate change. The first scenario is a spatially uniform temperature change and a uniform evaporation sensitivity that scales at the global-mean rate, reflecting the well-known approximations of Held and Soden (2006); the second scenario includes the impact of polar amplification of temperature change, as represented by a moist-static energy balance model (Roe et al. 2015; Siler et al. 2018); and the third scenario includes the strong temperature dependence of evaporation sensitivity, which is derived from the Penman surface energy balance equation (Siler et al. 2019).

Our main interest is what controls the temporal regression slope between $\overline{\delta_p}$ (in ^{18}O) and T_s at high latitudes, since variability in δ_p in ice cores is widely used for paleothermometry. For each scenario, we compute the temporal slope at each latitude based on the change in $\overline{\delta_p}$ that results from a global-mean cooling representative of the Last Glacial Maximum (LGM), and compare our result with independent estimates of the temporal slope based on analyses of ice cores from Greenland and Antarctica. Throughout this analysis, we will use the notation $[]'$ to indicate the change in a variable relative to its modern-day value.

a. Scenario 1: Uniform temperature change and uniform evaporation sensitivity

The analyses for the first scenario are presented in Fig. 3. We impose a spatially uniform cooling of $T'_s = -5$ K (Fig. 3a), which roughly approximates the global-mean temperature of the LGM (e.g., Shakun and Carlson 2010; Shakun et al. 2012; Annan and Hargreaves 2015; Tierney et al. 2020). The patterns of hydrologic change are shown in Fig. 3b, which we computed using two

280 approximations from Held and Soden (2006, hereafter HS06). First, if the atmospheric circulation
 281 stays about the same, F will roughly scale with atmospheric water vapor, which changes with T_s at
 282 the Clausius-Clapeyron rate of around 7 % K^{-1} :

$$F' \approx 0.07FT'_s. \quad (20)$$

283 As long as T'_s is relatively uniform, the same scaling also applies to $E - P$ (Fig. 3b, black line):

$$E' - P' \approx 0.07(E - P)T'_s. \quad (21)$$

284 Second, to separate $E' - P'$ into its component parts, we assume that E scales with T_s at the
 285 global-mean rate of 2 % K^{-1} everywhere, thus essentially preserving its zonal-mean pattern (Fig.
 286 3b, red line):

$$E' \approx .02ET'_s. \quad (22)$$

287 From Eqs. 21 and 22, the change in P (Fig. 3b, blue line) is then given by

$$P' \approx (.07P - .05E)T'_s. \quad (23)$$

288 Despite their simplicity, the HS06 approximations have been shown to capture important aspects of
 289 the hydrologic response in GCM simulations of greenhouse warming, including the amplification
 290 of the mean-state $E - P$ pattern (i.e., “wet gets wetter, dry gets drier”) and the decrease in subtropical
 291 P (HS06), making them a useful benchmark against which more sophisticated approximations will
 292 later be compared.

293 Fig. 3c shows the predicted change in $\overline{\delta_p}$ caused by the patterns of hydroclimate change in Figs.
 294 3a and 3b. Comparing these changes with the mean-state pattern of $\overline{\delta_p}$ in Fig. 2c, we find that
 295 $\overline{\delta_p}$ generally decreases with cooling in the subtropics, where mean-state values are relatively high,
 296 and increases in the deep tropics and at high latitudes, where mean-state values are relatively low.
 297 In other words, cooling results in a flattening of the meridional $\overline{\delta_p}$ gradient.

298 To estimate the temporal slope ($d\overline{\delta_p}/dT_s$), we divide the pattern of $\overline{\delta_p}'$ in Fig. 3c by the pattern of
 299 T_s' in Fig. 3a. The result, shown in Fig. 3d (black line), indicates positive slopes at low-to-middle
 300 latitudes and negative slopes poleward of $\sim 60^\circ$ in both hemispheres. We find a similar result if we
 301 assume that fractionation is fixed at 10 ‰ (Fig. 3d, gray line), implying that the temporal slope
 302 is mostly driven by changes in $\bar{\tau}$ resulting from E' and P' , and not by the temperature-dependence
 303 of fractionation. Significantly, the negative slopes at high latitudes contradict estimates of the
 304 temporal slope inferred from polar ice cores, which are all positive (Fig. 3d, symbols; Table A1
 305 and Appendix A4).

306 To understand why cooling causes $\bar{\tau}$ to decrease (and $\overline{\delta_p}$ to increase) at high latitudes in this
 307 scenario, recall that the hydrologic attenuation coefficient μ is proportional to P/F (Eq. 5). Under
 308 uniform global cooling, Eqs. 20 and 23 imply that P will decrease at a lower rate than F :

$$\frac{1}{P} \frac{dP}{dT_s} < \frac{1}{F} \frac{dF}{dT_s}. \quad (24)$$

309 As a result, μ will generally increase with cooling. And because μ represents an inverse transport
 310 length scale, an increase in μ implies that water vapor will travel a shorter distance on average
 311 before condensing. This is confirmed in the third row of Fig. 3, which shows a more localized
 312 distribution of precipitation resulting from evaporation at 40° latitude (w_e ; Fig. 3e), and a global-
 313 scale decrease in the average distance that vapor travels after evaporating ($\overline{d_e}$; Fig. 3f). This result
 314 is consistent with GCM simulations, which show an increase in vapor transport distance in response
 315 to anthropogenic global warming (Singh et al. 2016b). It also suggests a decrease in atmospheric
 316 residence time, provided that changes in atmospheric dynamics are small by comparison (Trenberth
 317 1998; Singh et al. 2016b).

318 An increase in μ with cooling has two competing effects on $\bar{\tau}$, which reflect opposing changes
 319 in τ and w_p (the two terms on the RHS of Eq. 19). On one hand, $\tau(x_1, x_2)$ increases, reflecting

320 the fact that vapor on average travels a shorter distance before condensing. Therefore, if we only
321 consider the component of local precipitation that evaporates at a single latitude, we would expect
322 $\bar{\tau}$ to *increase* in a cooler climate (and $\overline{\delta_p}$ to *decrease*), consistent with the conventional Rayleigh
323 understanding of the temperature effect (Dansgaard 1964).

324 On the other hand, μ also affects where vapor at a given latitude originates, as shown in the
325 fourth row of Fig. 3. Given a uniform fractional change in E (as implied by Eq. 22 under uniform
326 cooling), an increase in μ makes $w_p(x_1, x_2)$ more localized (Fig. 3g), implying that water vapor
327 originates from closer by (Fig. 3h). And since heavy isotopes become more depleted the farther
328 vapor travels along a given pathway, this contraction of $w_p(x_1, x_2)$ causes $\bar{\tau}$ to *decrease* in a cooler
329 climate (and $\overline{\delta_p}$ to *increase*).

330 To understand which effect dominates and where, it is helpful to consider the limit of weak vapor
331 transport, in which $F \rightarrow 0$ and $\mu \rightarrow \infty$. Applied to Eq. 19, this limit yields $\bar{\tau} = 1$ everywhere
332 (see Appendix A5). Under uniform global cooling, an increase in μ tends to nudge $\bar{\tau}$ toward this
333 weak-transport limit. In other words, $\bar{\tau}$ tends to increase with cooling in the subtropics, where
334 $\bar{\tau}(x) < 1$, and decrease with cooling in the deep tropics and at high latitudes, where $\bar{\tau}(x) > 1$.
335 This results in a flattening of the meridional gradients in both $\bar{\tau}$ and $\overline{\delta_p}$, explaining the negative
336 regression slope between $\overline{\delta_p}$ and T_s at high latitudes. That this result contradicts observational
337 estimates of the temporal slope from polar ice cores suggests that some important physics must be
338 missing from our approximations of hydroclimate change in this scenario.

339 *b. Scenario 2: Polar amplification*

340 The analyses for the second scenario are presented in Fig. 4. We keep the HS06 approximation
341 for evaporation sensitivity (Eq. 22), but use a moist energy balance model (MEBM; Roe et al.
342 2015; Siler et al. 2018; Bonan et al. 2018; Armour et al. 2019) to calculate spatial patterns of T'_s

343 and $E' - P'$. The MEBM assumes a down-gradient transport of near-surface moist static energy
344 and incorporates a Hadley Cell parameterization that gives it a realistic hydrologic cycle (Siler
345 et al. 2018). When forced with zonal-mean patterns of radiative forcing, feedbacks, and ocean heat
346 uptake diagnosed from GCMs, the MEBM replicates most of the spatial structure of T'_s and $E' - P'$
347 simulated by the GCMs in response to increasing atmospheric CO₂ (Siler et al. 2018).

348 In this scenario, we impose a spatially uniform feedback of $\lambda = -1 \text{ Wm}^{-2}\text{K}^{-1}$ and a spatially
349 uniform radiative forcing of -5 Wm^{-2} . This produces the same magnitude of global-mean cooling
350 that we prescribed in the HS06 analysis (-5 K), but with significant polar amplification (Fig. 4a),
351 reflecting a decrease in poleward latent heat transport as the meridional vapor gradient decreases
352 under global cooling (Roe et al., 2015). As a result of polar amplification, the patterns of E' and
353 P' also exhibit larger changes at high latitudes and smaller changes at low latitudes relative to the
354 uniform-warming scenario (Fig. 4b).

355 By itself, however, polar amplification does not fundamentally change the spatial patterns of $\overline{\delta_p'}$
356 or the temporal slope (Fig. 4c,d). From the source perspective, μ still increases nearly everywhere,
357 reducing the average distance vapor travels after evaporating (Fig. 4e,f). Likewise, from the sink
358 perspective, there is a broad decrease in the average distance that precipitation at a given latitude
359 travels from its source (Fig. 4g,h). As in the uniform-warming scenario, these changes in vapor
360 transport contribute to a flattening of the spatial patterns of $\overline{\delta_p'}$ and $\overline{\tau}$ under cooling. This implies
361 a negative temporal slope at high latitudes in contradiction to ice-core estimates (Fig. 4c,d),
362 suggesting that an important piece of physics must still be missing.

363 *c. Scenario 3: Temperature-dependent evaporation sensitivity*

364 The analyses for the third scenario are presented in Fig. 5. In this scenario we again use the
365 MEBM, but now also include a final piece of physics: a change in the spatial pattern of evaporation,

366 as derived from the Penman equation (Penman 1948; Siler et al. 2019). Using this equation, Siler
 367 et al. (2019) showed that the zonal-mean change in evaporation in CMIP5 simulations of global
 368 warming is well approximated as

$$E' \approx -\frac{R'_s - G'}{1 + \beta_0} + \frac{ET'_s \beta_0 (\tilde{\alpha} - 2/T_s)}{1 + \beta_0}, \quad (25)$$

369 where R'_s is the change in net downwelling radiation at the surface, G' is the change in ocean heat
 370 uptake/divergence,

$$\beta_0(T_s) = \frac{c_p}{\alpha L q^*(T_s)} \quad (26)$$

371 is the Bowen ratio in the limit of a saturated near-surface atmosphere,

$$\tilde{\alpha}(T_s) = \frac{L}{R^* T_s^2} \quad (27)$$

372 is the Clausius-Clapeyron scaling factor, q^* is the saturation specific humidity, and R^* is the specific
 373 gas constant of water vapor.

374 The first term on the RHS of Eq. 25 represents the contribution from the change in available
 375 energy at the surface ($R'_s - G'$). In radiative equilibrium, $G' = 0$ in the global mean, and can
 376 be neglected entirely if we assume a similar ocean circulation between the two climate states.
 377 Similarly, while R'_s is generally positive in GCM simulations of global warming, it has been shown
 378 to have minimal influence on the zonal-mean pattern of E' (Siler et al. 2018, 2019). For this reason,
 379 we follow Siler et al. (2018) and set $R'_s = 0$ as well.

380 That leaves the second term on the RHS of Eq. 25, which represents a thermodynamic con-
 381 straint on the partitioning between latent and sensible heat fluxes. It corresponds to an evaporation
 382 sensitivity E'/ET'_s that decreases nearly linearly with T_s (Supplemental Fig. 4), implying that evap-
 383 oration is most sensitive to temperature change at high latitudes, where the mean-state temperature
 384 is coolest (Scheff and Frierson 2014; Siler et al. 2019). The result is a larger decrease in E at high

latitudes and a smaller decrease at low latitudes compared to the HS06 approximation (Fig. 5b vs. Fig. 4b, red lines; see also Fig. 8 from Siler et al. 2018).

From the source perspective, the polar-amplification of E' implied by Eq. 25 has only a modest effect on vapor transport distance. As in the previous two scenarios, $\overline{d_e}$ decreases nearly everywhere (Fig. 5f), indicating that vapor travels a shorter distance from its source under cooling.

From the sink perspective, however, the polar-amplification of E' has a large impact (Fig. 5g,h). At high latitudes, in particular, the large decrease in E' locally means that precipitation comes from more remote regions on average, and thus travels a greater distance from its evaporation source, as indicated by an increase in $\overline{d_p}$ (Fig. 5h). Combined with the decrease in $\delta_p(x_1, x_2)$ caused by greater attenuation, this increase in average transport distance results in a large decrease in $\overline{\delta_p}$ at high latitudes (Fig. 5c), in stark contrast to the previous two scenarios (Figs. 3c and 4c). The decrease in $\overline{\delta_p}$ implies a positive temporal slope that is within the range of ice-core estimates, albeit on the low end in Antarctica (Fig. 5d). Greater slopes over Antarctica might be achieved by accounting for the role of sea ice, whose expansion under cooling would likely result in a further suppression of high-latitude E and a greater depletion of high-latitude δ_p . In any case, the similarity between the gray and black lines in Fig. 5d confirms that the positive temporal slope is well represented by changes in the average path-integrated attenuation ($\overline{\tau}$), implying that changes in the temperature-dependent fractionation factor (α) play only a secondary role.

These results highlight an important distinction between the source and sink definitions of vapor transport distance. From the source perspective, transport distance is proportional to μ^{-1} , which decreases robustly with cooling. From the sink perspective, however, transport distance is set by the shape of w_p , which is quite sensitive to the spatial pattern of E (Eq. 8). Because E is most sensitive to temperature change at high latitudes, the distribution of vapor sources shifts equatorward under

408 cooling. Thus, precipitation at high latitudes can originate from farther away under cooling, even
409 as vapor on average travels a shorter distance from where it evaporates.

410 **5. Source of hemispheric asymmetry in the temporal slope**

411 A striking aspect of the simulated temporal slope in Fig. 5d is that it accurately captures the
412 differences in observed temporal slopes between Antarctica, where the average exceeds 1 ‰ K^{-1} ,
413 and Greenland, where the average is around 0.4 ‰ K^{-1} (Table A1). Here we show that this
414 asymmetry can be explained by hemispheric differences in the mean-state meridional temperature
415 gradient.

416 Fig. 6a shows the annual-mean, zonal-mean surface temperature in the modern climate (blue
417 line), along with the local sensitivity of evaporation to temperature change (E'/ET'_s) given by
418 Eq. 25 with $G' = 0$ (solid red line). Poleward of about 65 degrees, the Southern Hemisphere
419 is significantly cooler than the Northern Hemisphere. While this asymmetry can be attributed
420 in part to the Antarctic continent, similar differences exist over high-latitude oceans, where most
421 evaporation occurs (Supplemental Fig. 5). Because evaporation is most sensitive to temperature
422 change at cool temperatures, this results in a larger meridional gradient in E'/ET'_s in the Southern
423 Hemisphere than in the Northern Hemisphere. Therefore, given similar patterns of cooling in each
424 hemisphere (Fig. 5a), the Southern Hemisphere will exhibit a larger equatorward shift in the spatial
425 pattern of evaporation, contributing to larger shifts in the distribution of evaporation sources at
426 high latitudes (Figs. 5g and 5h).

427 To test whether this effect can explain the hemispheric asymmetry in the temporal slope, we
428 repeat our analysis of Scenario 3, but adjust E' so that the pattern of E'/ET'_s is hemispherically
429 symmetric (Fig. 6a, dashed red line). As expected, the resulting temporal slope (Fig. 6b) exhibits
430 almost no difference between the Northern and Southern Hemispheres at high latitudes. This

431 confirms that the hemispheric differences in the high-latitude temporal slope in Scenario 3 (Fig.
432 5d) are indeed primarily the result of differences in the spatial pattern of evaporation change caused
433 by differences in the mean-state meridional temperature gradient.

434 **6. Sensitivity of the temporal slope to spatially varying feedbacks**

435 In Section 4, our MEBM simulation of the LGM climate used in Scenarios 2 and 3 assumed
436 a spatially uniform radiative feedback of $-1 \text{ Wm}^{-2}\text{K}^{-1}$. In GCMs, however, feedbacks usually
437 exhibit significant spatial variability, which can have a large impact on the patterns of E' , P' , and
438 T'_y .

439 Here we test the sensitivity of the temporal slope to different feedback patterns by repeating
440 our MEBM simulation of the LGM climate using the actual feedback patterns from 20 different
441 GCMs, which we computed using the same method described in Siler et al. (2018). Because these
442 feedback patterns are diagnosed from simulations of greenhouse warming, they likely misrepresent
443 aspects of the radiative response to global cooling, particularly related to changes in ice albedo.
444 Nevertheless, this approach provides a simple test of the robustness of our results given large model
445 uncertainties in the spatial patterns of feedbacks and hydroclimate change.

446 Figure 7a shows the patterns of temperature change simulated by the MEBM given the same
447 radiative forcing as before (-5 Wm^{-2}), but with spatially varying feedbacks diagnosed from
448 each GCM, which we have scaled to give a constant global-mean value of $-1 \text{ Wm}^{-2}\text{K}^{-1}$. The
449 ensemble-mean response is shown in yellow, while the individual models are sorted according to
450 the asymmetry of their temperature response, with deep blue indicating much more cooling in the
451 Northern Hemisphere, and deep red indicating roughly equal cooling in both hemispheres.

452 Figure 7b shows the range of temporal slopes given by the different feedback patterns when we
453 use the HS06 approximation for E' , as in Scenario 2. For all feedback patterns, the temporal slope

454 is essentially unchanged from the uniform-feedback case (Fig. 4d). This shows that, given uniform
455 evaporation scaling, varying patterns of feedbacks and temperature change are not sufficient to
456 produce high-latitude temporal slopes that are consistent with the ice-core record.

457 In contrast, when we apply the Penman evaporation scaling from Eq. 25, we find that most
458 feedback patterns yield temporal slopes that agree well with observations at high latitudes (Fig. 7c).
459 Interestingly, the feedback patterns that give the worst agreement with observations are associated
460 with much greater cooling in the Northern Hemisphere than in the Southern Hemisphere (deep
461 blue lines). However, feedback-driven differences in the temporal slope are small compared with
462 those resulting from different representations of evaporation change (Fig. 7b vs. Fig. 7c). This
463 reinforces our conclusion from Section 4c that the positive temporal slopes recorded in polar ice
464 cores largely reflect shifts in the spatial pattern of evaporation with climate change.

465 **7. Conclusion**

466 In this paper, we have introduced a simple framework for quantifying the movement of water vapor
467 and the spatial distribution of water isotopes within the zonal-mean climate. This framework is
468 based on the fact that horizontal vapor transport within the atmosphere is attenuated by precipitation
469 in much the same way that radiation is attenuated by scattering or absorption. In the zonal-mean
470 hydrologic cycle, we find that the attenuation coefficient μ is proportional to $P/|F|$, or the ratio of
471 precipitation to meridional vapor transport, and can therefore be determined from the zonal-mean
472 patterns of P and evaporation (E).

473 After finding μ , we use Beer's Law to derive the hydrologic transmittance $f(x_1, x_2)$, which
474 represents the fraction of water vapor that evaporates at a particular source latitude x_1 and reaches
475 a particular sink latitude x_2 without precipitating. From f , we can estimate where vapor that
476 evaporates at a particular latitude precipitates, and also where vapor that precipitates at a particular

477 latitude evaporates. These distributions allow us to estimate the average meridional distance that
478 vapor travels *from* a particular *source* latitude, as well as *to* a particular *sink* latitude. While the
479 former is roughly proportional to μ^{-1} , the latter is strongly dependent on the spatial pattern of E .

480 Combining this radiative-transfer framework with a Rayleigh distillation model then allows us
481 to solve for the zonal-mean δ of precipitation ($\overline{\delta_p}$). We focus on $\delta^{18}\text{O}$ in this study, but our
482 equations can easily be adapted for other meteoric isotopes like ^2H (deuterium) or ^{17}O . We account
483 for the influence of temperature and non-equilibrium kinetic effects on fractionation during both
484 evaporation and condensation, but at least for $\delta^{18}\text{O}$, we find that these effects are much less
485 important than attenuation, which is set by the zonal-mean patterns of E and P . This supports
486 the idea that variations in $\overline{\delta_p}$ are largely driven by local and remote imbalances in $E - P$, as several
487 recent studies have suggested (e.g., Lee et al. 2008; Moore et al. 2014; Bailey et al. 2018).

488 Finally, we consider the factors that contribute to the observed temporal regression slope between
489 $\overline{\delta_p}$ and temperature in polar ice cores. We simulate the response of $\overline{\delta_p}$ to three idealized patterns of
490 hydroclimate change, all associated with a 5 K decrease in global-mean temperature representative
491 of the Last Glacial Maximum. In each scenario, we find that μ increases with cooling because
492 F decreases at a greater rate than P . If we assume that the spatial pattern of E stays about the
493 same, an increase in μ results in a more uniform distribution of $\overline{\delta_p}$ across the globe. At high
494 latitudes, this implies a negative temporal regression slope between $\overline{\delta_p}$ and temperature, which
495 contradicts estimates derived from polar ice cores. That the temporal slope is in fact positive at
496 high latitudes thus requires a shift in E toward the tropics under global cooling and toward the
497 poles under global warming. We demonstrate that this shift can be explained by thermodynamic
498 constraints on the partitioning between latent and sensible heat fluxes, as predicted by the Penman
499 equation. However, we acknowledge that other factors may also play a role, including changes in
500 ocean circulation, the latitude of the midlatitude storm tracks (e.g., Aemisegger and Papritz 2018;

501 Aemisegger 2018), and especially sea ice extent (e.g., Noone and Simmonds 2004; Singh et al.
502 2017). Further research is needed to assess the relative importance of these factors.

503 Our analyses demonstrate that the $\delta^{18}\text{O}$ -temperature relationship at high latitudes reflects the
504 coherent response of temperature, heat transport, and hydrology over large spatial scales. While
505 traditional explanations of the $\delta^{18}\text{O}$ -temperature relationship tend to focus on how temperature
506 change alters the progressive fractionation of isotopes, our analyses show that the changing pattern
507 of evaporation also plays an essential role.

508 This result points to a potential limitation of ^{18}O paleothermometry that we have not directly
509 addressed here: namely, a decrease in $\delta^{18}\text{O}$ in ice cores need not necessarily be accompanied
510 by global- or even local-scale cooling, but could in principle result from *any* event that dispro-
511 portionately reduces high-latitude evaporation. For example, one could imagine past episodes of
512 hemisphere- or basin-specific expansions in sea ice that were driven not by cooling, but by regional
513 changes in ocean dynamics, salinity, or stratification (e.g., Bintanja et al. 2015; Pauling et al. 2016,
514 2017). Distinguishing the isotopic signatures of such processes from those of local and global
515 temperature variability is an important avenue for future research.

516 *Acknowledgments.* We thank Stefan Terzer-Wassmuth for help accessing the IAEA/GNIP
517 database. We thank Mathieu Casado and two anonymous reviewers for very helpful suggestions.
518 NS was supported by NSF grant AGS-1954663. CB was supported by NSF grants ANT-1643394
519 and ARC-1804154. DN was supported by NSF grant AGS-1502806. This material is based
520 upon work supported by the National Center for Atmospheric Research, which is a major facility
521 sponsored by the National Science Foundation under Cooperative Agreement No. 1852977.

522 *Data availability statement.* ERA5 monthly-mean evaporation, precipitation, and 2-m air temper-
523 ature over the period 1979-2018 are available at <https://climate.copernicus.eu/climate-reanalysis>.

524 Temperature and energy fluxes from the fifth-generation Coupled Model Intercomparison Project
525 (CMIP5) are available at <https://esgf-node.llnl.gov/search/cmip5/>. Observations of precipitation
526 $\delta^{18}\text{O}$ are available at <https://www.iaea.org/services/networks/gnip>. Observational estimates of
527 the temporal regression slope between $\delta^{18}\text{O}$ and temperature in polar ice cores were taken from
528 publications cited in Table A1.

529 APPENDIX

530 A1. Approximation of $\overline{d_e}(x_1)$ in Eq. 10

531 Over most of the globe, $\mu(x)$ varies much less over small scales than does $f(x_1, x_2)$, which
532 exhibits exponential decay (Eq. 4). If we assume that μ is approximately constant over the length
533 scale of $f(x_1, x_2)$, then we can approximate Eq. 7 as

$$w_e(x_1, x_2) \approx \mu(x_1)e^{-\tau(x_1, x_2)}. \quad (\text{A1})$$

534 Similarly, the distance between source and sink latitudes is approximately

$$a|\theta_2 - \theta_1| \approx \frac{a|x_2 - x_1|}{\cos\theta_1}, \quad (\text{A2})$$

535 based on the relation $dx = d\theta \cos\theta$. For simplicity, let us assume that $x_2 > x_1$, meaning that vapor
536 transport is northward at the source latitude. Substituting Eqs. A1 and A2 into Eq. 9 then gives

$$\overline{d_e}(x_1) \approx \frac{a\mu(x_1)}{\cos\theta_1} \int_{x_1}^1 (x_2 - x_1)e^{-\tau(x_1, x_2)} dx_2. \quad (\text{A3})$$

537 To evaluate this integral, we substitute $x_2 - x_1 \approx \mu(x_1)^{-1}\tau(x_1, x_2)$ and $dx_2 \approx \mu(x_1)^{-1}d\tau$. These
538 approximations derive from Eq. 2, based again on the assumption that $\mu(x_2) \approx \mu(x_1)$ over relevant
539 transport scales. Because $F = 0$ at the poles, $\tau = \infty$ at $x_2 = 1$, while $\tau = 0$ at $x_2 = x_1$. Therefore, we
540 integrate from $\tau = 0$ to ∞ :

$$\overline{d_e}(x_1) \approx \frac{a\mu(x_1)}{\cos\theta_1} \frac{1}{\mu(x_1)^2} \int_0^\infty \tau e^{-\tau} d\tau. \quad (\text{A4})$$

541 The integral in Eq. A4 is equal to 1, yielding the approximation for $\overline{d_e}(x_1)$ in Eq. 10. The same
 542 result can be shown to apply for southward transport in which $x_2 < x_1$.

543 A2. Temperature-dependence of α

544 When the effective fractionation factor for condensation (α) depends on the condensation tem-
 545 perature T_c , $R_p(x_1, x_2)$ is approximately equal to (Dansgaard 1964)

$$R_p(x_1, x_2) \approx \alpha(\overline{T_c}[x_2])R_e(x_1)f(x_1, x_2)\overline{\alpha}(x_1, x_2)^{-1}. \quad (\text{A5})$$

546 Here α is the effective fractionation factor of condensation, which we parameterize as a func-
 547 tion of the column-mean condensation temperature $\overline{T_c}(x_2)$, and $\overline{\alpha}(x_1, x_2)$ is the average effective
 548 fractionation factor over the lifetime of a vapor parcel that evaporates at x_1 and is transported to x_2 .

549 We approximate the column-mean condensation temperature as

$$\overline{T_c}(x) \approx \frac{\int_0^\infty T(x, z)C(x, z)dz}{\int_0^\infty C(x, z)dz}, \quad (\text{A6})$$

550 where $T(x, z)$ is the average vertical temperature profile at x during condensation and $C(x, z)$ is
 551 the condensation rate per distance of vertical displacement. To approximate these variables, we
 552 consider the idealized case of a saturated air parcel that ascends from the surface to the tropopause,
 553 which is a reasonable assumption during strong precipitating storms. In this scenario, equivalent
 554 potential temperature (θ_e) is conserved as a parcel ascends, implying that

$$C(x, z) = -\rho \frac{dq^*}{dz} \Big|_{\theta_e} \approx \rho \frac{dq^*}{dT} \Gamma_m, \quad (\text{A7})$$

555 where ρ is the air density, q^* is the saturation specific humidity, and $\Gamma_m = -dT/dz|_{\theta_e}$ is the moist
 556 adiabatic lapse rate. For $q^*(T)$, we use an approximate form of the Clausius–Clapeyron equation,

$$q^*(T) \approx q^*(T_s)e^{\tilde{\alpha}\Delta T}, \quad (\text{A8})$$

557 where $\Delta T = T - T_s$ and $\tilde{\alpha}(T_s)$ is the Clausius-Clapeyron scaling factor defined in Eq. 27. Differen-
 558 tiating Eq. A8 gives $dq^*/dT = \tilde{\alpha}q^*$, which we combine with Eq. A7 to get

$$C(x, z) \approx \rho \tilde{\alpha} q^* \Gamma_m. \quad (\text{A9})$$

559 We assume for simplicity that Γ_m is independent of z , implying that T decreases linearly with
 560 height:

$$T(x, z) \approx T_s(x) - \Gamma_m(x)z. \quad (\text{A10})$$

561 From Eqs. A8 and A10, the vertical profile of water vapor is then given by

$$q^*(x, z) \approx q^*(x, 0)e^{-\tilde{\alpha}\Gamma_m z}. \quad (\text{A11})$$

562 Finally, substituting Eqs. A9-A11 into A6 gives

$$\overline{T_c}(x) \approx T_s(x) - \tilde{\alpha}(T_s)^{-1}. \quad (\text{A12})$$

563 We approximate $\alpha(\overline{T_c})$ in Eq. A5 following previous models (e.g., Jouzel and Merlivat 1984;
 564 Petit et al. 1991; Ciais and Jouzel 1994; Hoffmann et al. 1998; Kavanaugh and Cuffey 2003).
 565 It is equal to the average of the fractionation factors for liquid and ice, weighted by the relative
 566 abundance of each species at a given condensation temperature:

$$\alpha(\overline{T_c}) = f_l(\overline{T_c})\alpha_l(\overline{T_c}) + [1 - f_l(\overline{T_c})]\alpha_i(\overline{T_c})\alpha_k(\overline{T_c}). \quad (\text{A13})$$

567 Here α_l and α_i are the temperature-dependent equilibrium fractionation factors for liquid-vapor
 568 and ice-vapor transitions, which we take from Majoube (1970, 1971); f_l is a weighting function
 569 representing the temperature-dependent fraction of total cloud water that is in the liquid phase,
 570 which Markle (2017) estimated from satellite observations; and α_k accounts for kinetic effects
 571 resulting from supersaturation at low temperatures.

572 To estimate α_k , we follow Jouzel and Merlivat (1984):

$$\alpha_k = \frac{S_i}{1 + \alpha_i \alpha_d (S_i - 1)}, \quad (\text{A14})$$

573 where $\alpha_d = 1.0285$ is the fractionation factor for molecular diffusion of snow and S_i is the super-
 574 saturation, which is parameterized as a linear function of $\overline{T_c}$ (in °C):

$$S_i = 1 - C\overline{T_c}. \quad (\text{A15})$$

575 Most previous studies have assumed values for C that range anywhere from 0.002 (e.g., Landais
 576 et al. 2008) to 0.008 (Schoenemann and Steig 2016). However, Markle (2017) has argued that
 577 values of C at the extremes of this range are inconsistent with the observed relationship between
 578 $\delta^{18}\text{O}$ and $\delta^2\text{H}$ in global precipitation. Following Markle (2017), we choose a value near the middle
 579 of this range ($C = 0.00525$), but note that values of 0.007 and 0.003 give broadly similar results
 580 for the high-latitude temporal slope as those presented in Section 4 (Supplemental Fig. 6). This
 581 parameterization yields the profile of $\alpha(T_c)$ shown in purple in Supplemental Fig. 2. We then
 582 smooth this curve to account for the spread in condensation temperatures about $\overline{T_c}$ at a given latitude
 583 (black line).

584 To approximate $\overline{\alpha}(x_1, x_2)$ in Eq. A5, we compute the average value of $\alpha(T_c)$ over the temperature
 585 range $T_s(x_1) < T_c < \overline{T_c}(x_2)$, weighted by the amount of condensation that occurs at each temperature
 586 (dq^*/dT_c). Because q^* is approximately exponential, $dq^*/dT_c \propto q^*(T_c)$, and the weighted average
 587 simplifies to

$$\overline{\alpha}(x_1, x_2) \approx \frac{\int_{T_s(x_1)}^{\overline{T_c}(x_2)} \alpha(T_c) q^*(T_c) dT_c}{\int_{T_s(x_1)}^{\overline{T_c}(x_2)} q^*(T_c) dT_c}. \quad (\text{A16})$$

588 A3. Implementation of the Craig-Gordon Model

589 The Craig-Gordon model (Craig and Gordon 1965) represents a simple parameterization of the
 590 influence of temperature and non-equilibrium kinetics on the isotope ratio of water vapor as it
 591 evaporates from the ocean surface. We implement it using the following equation (e.g., Hoffmann

592 et al. 1998; Lee et al. 2008):

$$\delta_e = \frac{\delta_o - h\delta_v + 1000(\alpha_e^{-1} - 1)}{1 - h} + \Delta_k, \quad (\text{A17})$$

593 where $\alpha_e(T_s)$ is the equilibrium fractionation factor for conversion from liquid to vapor, h is
594 the relative humidity with respect to sea-surface temperature, Δ_k is an empirical correction that
595 accounts for kinetic effects, and δ_e , δ_o , and δ_v represent the isotopic composition of the evaporative
596 flux, ocean water, and near-surface atmosphere, respectively. Each δ_x can be converted to an
597 isotope ratio R_x using Eq. 13. We set $r = 0.7$, $\delta_o = 0$, and $\Delta_k = -6$ ‰ (following Lee et al. 2008).

598 The remaining two variables, δ_e and δ_v , must be solved iteratively. Because δ_v depends on the
599 fractionation of vapor that evaporates upstream, we compute it as the weighted average of upstream
600 sources, analogous to $\overline{\delta_p}$ in Eq. 12. However, we recognize that the near-surface atmosphere is
601 more likely than the rest of the atmospheric column to contain vapor that evaporates locally. To
602 account for this, we replace $w_p(x_1, x_2)$ with a weighting function $w_v(x_1, x_2)$ that gives more weight
603 to local sources:

$$w_v(x_1, x_2) = \frac{f(x_1, x_2)^\kappa E(x_1)}{\int_{-1}^1 f(x_1, x_2)^\kappa E(x_1) dx_1}, \quad (\text{A18})$$

604 where κ is a free parameter. We have experimented with different values of κ ranging from 1
605 (which gives $w_v = w_p$) to 2. Comparing the resulting values of δ_v and δ_e in the modern climate
606 with Fig. 11 from Lee et al. (2008), we find the best agreement by setting $\kappa = 1.5$ (Supplemental
607 Fig. 3). This value is therefore used for all simulations.

608 **A4. Observational estimates of the temporal slope from polar ice cores**

609 The symbols shown in panel (d) of Figs. 3-5, panel (b) of Fig. 6, and panels (b) and (c) of Fig.
610 7 represent estimates of the temporal slope derived from analyses of water isotope variability in
611 polar ice cores, as summarized in Table A1. Because our analysis focuses on differences between

612 the LGM and the modern climate, we only consider slope estimates that are derived from direct
 613 analysis of ice-core variability over the last deglaciation (i.e., from the LGM to the Holocene). We
 614 do not consider estimates that are based on GCM simulations, spatial regression slopes, or ice-core
 615 analyses that do not span the last deglaciation.

616 All values of the temporal slope in Table A1 are taken directly from the published sources, with
 617 some caveats. First, in cases where only a $\delta^2\text{H}$ slope was published, we have divided that value by
 618 8 to make it comparable to the $\delta^{18}\text{O}$ slope. Second, the slope of 0.33‰ K^{-1} for the GRIP core that
 619 we attribute to Johnsen et al. (1995) is derived from their Eq. 1, using their parameters and their
 620 values of $dT_s/d\delta_p$ from the LGM and Holocene. Third, the slope of 0.38‰ K^{-1} for the NGRIP
 621 core that we attribute to Kindler et al. (2014) is derived from their Fig. 3a, which shows an increase
 622 in $\delta^{18}\text{O}$ of about 6‰ along with an increase in temperature of about 16 K between the LGM and
 623 the beginning of the Holocene. Finally, the study by Buizert et al. (2021), from which we get most
 624 of our Antarctic slope estimates, has not yet been published, but is currently in peer review.

625 A5. Evaluating $\bar{\tau}$ in the weak-transport limit

626 To find $\bar{\tau}$ in the limit of weak vapor transport ($F \rightarrow 0$), we begin with Eq. 19 and use the relation
 627 $d\tau/dx = \mu$ to change the variable of integration from dx_1 to $d\tau/\mu$. Because vapor only travels to
 628 x_2 from the upstream direction (determined by the sign of F), and because $\tau = \infty$ at the poles (see
 629 Appendix A1 above), we can write Eq. 19 as

$$\bar{\tau} = \frac{\int_0^\infty \tau \mu^{-1} E e^{-\tau} d\tau}{\int_0^\infty \mu^{-1} E e^{-\tau} d\tau}. \quad (\text{A19})$$

630 Here $\tau = 0$ at $x_1 = x_2$ (i.e., where the sink latitude equals the source latitude) and increases to
 631 infinity as x_1 moves further upstream.

632 As F decreases, μ increases, for reasons discussed in Section 4a. Therefore, the transmittance
633 ($f = e^{-\tau}$) decays more sharply (in physical space) away from the source latitude, reflecting a
634 decrease in transport length scale. By contrast, there is no mechanism that would cause the scale
635 of spatial variability in E or μ to decrease by a similar magnitude. Thus, as $F \rightarrow 0$, E and μ
636 become essentially constant over the transport length scale, and can therefore be brought outside
637 the integrals, where they cancel. Thus, in the weak-transport limit, Eq. 19 reduces to

$$\bar{\tau} \approx \frac{\int_0^{\infty} \tau e^{-\tau} d\tau}{\int_0^{\infty} e^{-\tau} d\tau} = 1. \quad (\text{A20})$$

638 Physically, this result is a necessary consequence of mass conservation. In the absence of horizontal
639 transport, δ_p must equal δ_e everywhere. Under constant fractionation, both will be equal to $-\epsilon$,
640 and thus $\bar{\tau}$ must equal 1 (Eq. 17).

641 References

- 642 Aemisegger, F., 2018: On the link between the North Atlantic storm track and precipitation
643 deuterium excess in Reykjavik. *Atmospheric Science Letters*, **19** (12), doi:10.1002/asl.865.
- 644 Aemisegger, F., and L. Papritz, 2018: A climatology of strong large-scale ocean evaporation events.
645 Part I: Identification, global distribution, and associated climate conditions. *J. Climate*, **31** (18),
646 doi:10.1175/JCLI-D-17-0591.1.
- 647 Allen, M., and W. J. Ingram, 2002: Constraints on future changes in climate and the hydrologic
648 cycle. *Nature*, **419** (6903), 224–232.
- 649 Annan, J., and J. Hargreaves, 2015: A perspective on model-data surface temperature compar-
650 ison at the Last Glacial Maximum. *Quaternary Science Reviews*, **107**, 1–10, doi:10.1016/J.
651 QUASCIREV.2014.09.019.

- 652 Armour, K. C., N. Siler, A. Donohoe, and G. H. Roe, 2019: Meridional Atmospheric Heat Transport
653 Constrained by Energetics and Mediated by Large-Scale Diffusion. *J. Climate*, **32** (12), 3655–
654 3680, doi:10.1175/JCLI-D-18-0563.1.
- 655 Bailey, A., E. Posmentier, and X. Feng, 2018: Patterns of Evaporation and Precipitation Drive
656 Global Isotopic Changes in Atmospheric Moisture. *Geophys. Res. Lett.*, **45** (14), 7093–7101,
657 doi:10.1029/2018GL078254.
- 658 Bintanja, R., G. J. Van Oldenborgh, and C. A. Katsman, 2015: The effect of increased fresh water
659 from Antarctic ice shelves on future trends in Antarctic sea ice. *Annals of Glaciology*, **56** (69),
660 doi:10.3189/2015AoG69A001.
- 661 Boer, G., 1993: Climate change and the regulation of the surface moisture and energy budgets.
662 *Climate Dynamics*, **8**, 225–239.
- 663 Bonan, D. B., K. C. Armour, G. H. Roe, N. Siler, and N. Feldl, 2018: Sources of Uncertainty
664 in the Meridional Pattern of Climate Change. *Geophys. Res. Lett.*, **45** (17), 9131–9140, doi:
665 10.1029/2018GL079429, URL <http://doi.wiley.com/10.1029/2018GL079429>.
- 666 Boyle, E. A., 1997: Cool tropical temperatures shift the global $\delta^{18}\text{O}$ -T relationship: An explanation
667 for the ice core $\delta^{18}\text{O}$ - borehole thermometry conflict? *Geophys. Res. Lett.*, **24** (3), 273–276,
668 doi:10.1029/97GL00081.
- 669 Buizert, C., and Coauthors, 2014: Greenland temperature response to climate forcing during the
670 last deglaciation. *Science (New York, N.Y.)*, **345** (6201), 1177–80, doi:10.1126/science.1254961.
- 671 Buizert, C., and Coauthors, 2021: Antarctic surface temperature and elevation during the Last
672 Glacial Maximum. *Science*, In Review.

- 673 Charles, C. D., D. Rind, J. Jouzel, R. D. Koster, and R. G. Fairbanks, 1994: Glacial-interglacial
674 changes in moisture sources for greenland: influences on the ice core record of climate. *Science*
675 (*New York, N.Y.*), **263 (5146)**, 508–11, doi:10.1126/science.263.5146.508.
- 676 Ciais, P., and J. Jouzel, 1994: Deuterium and oxygen 18 in precipitation: Isotopic model, including
677 mixed cloud processes. *J. Geophys. Res.: Atmos.*, **99 (D8)**, 16 793, doi:10.1029/94JD00412.
- 678 Craig, H., and L. Gordon, 1965: Deuterium and oxygen 18 variations in the ocean and the marine
679 atmosphere. *Stable Isotopes in Oceanographic Studies and Paleotemperatures*, E. Tongiorgi,
680 Ed., Lab. di Geol. Nucl., Pisa, Italy, 9–130.
- 681 Cuffey, K. M., R. B. Alley, P. M. Grootes, J. M. Bolzan, and S. Anandakrishnan, 1994: Calibration
682 of the $\delta^{18}\text{O}$ isotopic paleothermometer for central Greenland, using borehole temperatures.
683 *Journal of Glaciology*, **40 (135)**, 341–349, doi:10.3189/S0022143000007425.
- 684 Cuffey, K. M., G. D. Clow, R. B. Alley, M. Stuiver, E. D. Waddington, and R. W. Saltus, 1995: Large
685 Arctic Temperature Change at the Wisconsin-Holocene Glacial Transition. *Science*, **270 (5235)**,
686 455–458, doi:10.1126/science.270.5235.455.
- 687 Cuffey, K. M., and Coauthors, 2016: Deglacial temperature history of West Antarctica. *Proceedings*
688 *of the National Academy of Sciences of the United States of America*, **113 (50)**, 14 249–14 254,
689 doi:10.1073/pnas.1609132113.
- 690 Dahl-Jensen, D., K. Mosegaard, N. Gundestrup, G. D. Clow, S. J. Johnsen, A. W. Hansen, and
691 N. Balling, 1998: Past temperatures directly from the greenland ice sheet. *Science (New York,*
692 *N.Y.)*, **282 (5387)**, 268–71, doi:10.1126/science.282.5387.268.
- 693 Dansgaard, W., 1964: Stable isotopes in precipitation. *Tellus*, **16 (4)**, 436–468, doi:10.1111/j.
694 2153-3490.1964.tb00181.x.

- 695 Fisher, D. A., 1990: A Zonally-Averaged Stable-Isotope Model Coupled to a Regional
696 Variable-Elevation Stable-Isotope Model. *Annals of Glaciology*, **14**, 65–71, doi:10.3189/
697 S0260305500008284.
- 698 Galewsky, J., H. C. Steen-Larsen, R. D. Field, J. Worden, C. Risi, and M. Schneider, 2016:
699 Stable isotopes in atmospheric water vapor and applications to the hydrologic cycle. *Reviews of*
700 *Geophysics*, **54** (4), doi:10.1002/2015RG000512.
- 701 Grootes, P. M., M. Stuiver, J. W. C. White, S. Johnsen, and J. Jouzel, 1993: Comparison of oxygen
702 isotope records from the GISP2 and GRIP Greenland ice cores. *Nature*, **366** (6455), 552–554,
703 doi:10.1038/366552a0.
- 704 Held, I. M., and B. J. Soden, 2006: Robust Responses of the Hydrological Cycle to Global
705 Warming. *J. Climate*, **19** (21), 5686–5699.
- 706 Hersbach, H., and Coauthors, 2020: The ERA5 global reanalysis. *Quart. J. Roy. Meteor. Soc.*,
707 doi:10.1002/qj.3803.
- 708 Hoffmann, G., M. Werner, and M. Heimann, 1998: Water isotope module of the ECHAM atmo-
709 spheric general circulation model: A study on timescales from days to several years. *J. Geophys.*
710 *Res.: Atmos.*, **103** (D14), 16 871–16 896, doi:10.1029/98JD00423.
- 711 Johnsen, S. J., D. Dahl-Jensen, W. Dansgaard, and N. Gundestrup, 1995: Greenland palaeotemper-
712 atures derived from GRIP bore hole temperature and ice core isotope profiles. *Tellus B*, **47** (5),
713 624–629, doi:10.1034/j.1600-0889.47.issue5.9.x.
- 714 Johnsen, S. J., W. Dansgaard, and J. W. C. White, 1989: The origin of Arctic precipitation
715 under present and glacial conditions. *Tellus B*, **41B** (4), 452–468, doi:10.1111/j.1600-0889.
716 1989.tb00321.x.

- 717 Johnsen, S. J., and Coauthors, 2001: Oxygen isotope and palaeotemperature records from six
718 Greenland ice-core stations: Camp Century, Dye-3, GRIP, GISP2, Renland and NorthGRIP.
719 *Journal of Quaternary Science*, **16 (4)**, 299–307, doi:10.1002/jqs.622.
- 720 Jouzel, J., and L. Merlivat, 1984: Deuterium and oxygen 18 in precipitation: Modeling of the
721 isotopic effects during snow formation. *J. Geophys. Res.: Atmos.*, **89 (D7)**, 11 749, doi:10.1029/
722 JD089iD07p11749.
- 723 Jouzel, J., F. Vimeux, N. Caillon, G. Delaygue, G. Hoffmann, V. Masson-Delmotte, and F. Parrenin,
724 2003: Magnitude of isotope/temperature scaling for interpretation of central Antarctic ice cores.
725 *J. Geophys. Res.: Atmos.*, **108 (D12)**, 4361, doi:10.1029/2002JD002677.
- 726 Jouzel, J., and Coauthors, 1997: Validity of the temperature reconstruction from water isotopes in
727 ice cores. *J. Geophys. Res.: Oceans*, **102 (C12)**, 26 471–26 487, doi:10.1029/97JC01283.
- 728 Kavanaugh, J. L., and K. M. Cuffey, 2003: Space and time variation of $\delta^{18}\text{O}$ and δD in Antarctic
729 precipitation revisited. *Global Biogeochemical Cycles*, **17 (1)**, doi:10.1029/2002GB001910.
- 730 Kindler, P., M. Guillevic, M. Baumgartner, J. Schwander, A. Landais, and M. Leuenberger, 2014:
731 Temperature reconstruction from 10 to 120 kyr b2k from the NGRIP ice core. *Climate of the*
732 *Past*, **10 (2)**, 887–902, doi:10.5194/cp-10-887-2014.
- 733 Krinner, G., C. Genthon, and J. Jouzel, 1997: GCM analysis of local influences on ice core δ
734 signals. *Geophys. Res. Lett.*, **24 (22)**, 2825–2828, doi:10.1029/97GL52891.
- 735 Landais, A., E. Barkan, and B. Luz, 2008: Record of $\delta^{18}\text{O}$ and 17O -excess in ice from Vostok
736 Antarctica during the last 150,000 years. *Geophysical Research Letters*, **35 (2)**, doi:10.1029/
737 2007GL032096.

- 738 Lee, J.-E., I. Fung, D. J. DePaolo, and B. Otto-Bliesner, 2008: Water isotopes during the Last
739 Glacial Maximum: New general circulation model calculations. *J. Geophys. Res.: Atmos.*,
740 **113 (D19)**, D19 109, doi:10.1029/2008JD009859.
- 741 Majoube, M., 1970: Fractionation Factor of ^{18}O between Water Vapour and Ice. *Nature*,
742 **226 (5252)**, 1242–1242, doi:10.1038/2261242a0.
- 743 Majoube, M., 1971: Fractionnement en oxygène 18 et en deutérium entre l'eau et sa vapeur.
744 *Journal de Chimie Physique*, **68**, 1423–1436, doi:10.1051/jcp/1971681423.
- 745 Markle, B. R., 2017: Climate dynamics revealed in ice cores: advances in techniques, theory, and
746 interpretation. Ph.D. thesis, University of Washington.
- 747 Masson-Delmotte, V., 2005: GRIP Deuterium Excess Reveals Rapid and Orbital-Scale Changes
748 in Greenland Moisture Origin. *Science*, **309 (5731)**, 118–121, doi:10.1126/science.1108575.
- 749 Masson-Delmotte, V., and Coauthors, 2006: Past temperature reconstructions from deep ice
750 cores: relevance for future climate change. *Climate of the Past*, **2 (2)**, 145–165, doi:10.5194/
751 cp-2-145-2006.
- 752 Moore, M., Z. Kuang, and P. N. Blossey, 2014: A moisture budget perspective of the amount effect.
753 *Geophys. Res. Lett.*, **41 (4)**, 1329–1335, doi:10.1002/2013GL058302.
- 754 Noone, D., and I. Simmonds, 2004: Sea ice control of water isotope transport to Antarctica
755 and implications for ice core interpretation. *J. Geophys. Res.: Atmos.*, **109 (D7)**, D07 105,
756 doi:10.1029/2003JD004228.
- 757 Pauling, A. G., C. M. Bitz, I. J. Smith, and P. J. Langhorne, 2016: The response of the Southern
758 Ocean and Antarctic sea ice to freshwater from ice shelves in an earth system model. *Journal of*
759 *Climate*, **29 (5)**, doi:10.1175/JCLI-D-15-0501.1.

- 760 Pauling, A. G., I. J. Smith, P. J. Langhorne, and C. M. Bitz, 2017: Time-Dependent Freshwater
761 Input From Ice Shelves: Impacts on Antarctic Sea Ice and the Southern Ocean in an Earth
762 System Model. *Geophysical Research Letters*, **44** (20), doi:10.1002/2017GL075017.
- 763 Penman, H. L., 1948: Natural Evaporation from Open Water, Bare Soil and Grass. *Proceedings of*
764 *the Royal Society A: Mathematical, Physical and Engineering Sciences*, **193** (1032), 120–145,
765 doi:10.1098/rspa.1948.0037.
- 766 Petit, J. R., J. W. White, N. W. Young, J. Jouzel, and Y. S. Korotkevich, 1991: Deuterium excess
767 in recent Antarctic snow. *Journal of Geophysical Research*, **96** (D3), doi:10.1029/90JD02232.
- 768 Rhines, A., and P. J. Huybers, 2014: Sea Ice and Dynamical Controls on Preindustrial and Last
769 Glacial Maximum Accumulation in Central Greenland. *J. Climate*, **27** (23), 8902–8917, doi:
770 10.1175/JCLI-D-14-00075.1.
- 771 Roe, G. H., N. Feldl, K. C. Armour, Y.-T. Hwang, and D. M. W. Frierson, 2015: The remote
772 impacts of climate feedbacks on regional climate predictability. *Nature Geoscience*, **8** (2), 135–
773 139, doi:10.1038/ngeo2346.
- 774 Salamatina, A. N., V. Y. Lipenkov, N. I. Barkov, J. Jouzel, J. R. Petit, and D. Raynaud, 1998: Ice
775 core age dating and paleothermometer calibration based on isotope and temperature profiles
776 from deep boreholes at Vostok Station (East Antarctica). *J. Geophys. Res.: Atmos.*, **103** (D8),
777 8963–8977, doi:10.1029/97JD02253.
- 778 Scheff, J., and D. M. W. Frierson, 2014: Scaling potential evapotranspiration with greenhouse
779 warming. *J. Climate*, **27** (4), 1539–1558, doi:10.1175/JCLI-D-13-00233.1.

- 780 Schoenemann, S. W., and E. J. Steig, 2016: Seasonal and spatial variations of ^{17}O excess and
781 $\delta^{18}\text{O}$ in Antarctic precipitation: Insights from an intermediate complexity isotope model.
782 *Journal of Geophysical Research*, **121** (19), doi:10.1002/2016JD025117.
- 783 Severinghaus, J. P., T. Sowers, E. J. Brook, R. B. Alley, and M. L. Bender, 1998: Timing of abrupt
784 climate change at the end of the Younger Dryas interval from thermally fractionated gases in
785 polar ice. *Nature*, **391** (6663), 141–146, doi:10.1038/34346.
- 786 Shakun, J. D., and A. E. Carlson, 2010: A global perspective on Last Glacial Maximum to
787 Holocene climate change. *Quaternary Science Reviews*, **29** (15-16), 1801–1816, doi:10.1016/J.
788 QUASCIREV.2010.03.016.
- 789 Shakun, J. D., and Coauthors, 2012: Global warming preceded by increasing carbon dioxide con-
790 centrations during the last deglaciation. *Nature*, **484** (7392), 49–54, doi:10.1038/nature10915.
- 791 Siler, N., G. H. Roe, and K. C. Armour, 2018: Insights into the Zonal-Mean Response of the
792 Hydrologic Cycle to Global Warming from a Diffusive Energy Balance Model. *J. Climate*,
793 **31** (18), 7481–7493, doi:10.1175/JCLI-D-18-0081.1.
- 794 Siler, N., G. H. Roe, K. C. Armour, and N. Feldl, 2019: Revisiting the surface-energy-flux
795 perspective on the sensitivity of global precipitation to climate change. *Climate Dynamics*,
796 **52** (7-8), 3983–3995, doi:10.1007/s00382-018-4359-0.
- 797 Singh, H. A., C. M. Bitz, J. Nusbaumer, and D. C. Noone, 2016a: A mathematical framework for
798 analysis of water tracers: Part 1: Development of theory and application to the preindustrial
799 mean state. *Journal of Advances in Modeling Earth Systems*, **8** (2), 991–1013, doi:10.1002/
800 2016MS000649.

- 801 Singh, H. K., C. M. Bitz, A. Donohoe, and P. J. Rasch, 2017: A source-receptor perspective on the
802 polar hydrologic cycle: Sources, seasonality, and arctic-antarctic parity in the hydrologic cycle
803 response to CO₂ doubling. *J. Climate*, **30** (24), 9999–10 017, doi:10.1175/JCLI-D-16-0917.1.
- 804 Singh, H. K. A., C. M. Bitz, A. Donohoe, J. Nusbaumer, and D. C. Noone, 2016b: A Mathematical
805 Framework for Analysis of Water Tracers. Part II: Understanding Large-Scale Perturbations in
806 the Hydrological Cycle due to CO₂ Doubling. *J. Climate*, **29** (18), 6765–6782, doi:10.1175/
807 JCLI-D-16-0293.1.
- 808 Sodemann, H., C. Schwierz, and H. Wernli, 2008: Interannual variability of Greenland winter
809 precipitation sources: Lagrangian moisture diagnostic and North Atlantic Oscillation influence.
810 *J. Geophys. Res.: Atmos.*, **113** (D3), D03 107, doi:10.1029/2007JD008503.
- 811 Sodemann, H., and A. Stohl, 2009: Asymmetries in the moisture origin of Antarctic precipitation.
812 *Geophys. Res. Lett.*, **36** (22), L22 803, doi:10.1029/2009GL040242.
- 813 Tierney, J. E., J. Zhu, J. King, S. B. Malevich, G. J. Hakim, and C. J. Poulsen, 2020: Glacial
814 cooling and climate sensitivity revisited. *Nature*, **584** (7822), doi:10.1038/s41586-020-2617-x.
- 815 Trenberth, K. E., 1998: Atmospheric Moisture Residence Times and Cycling: Implications
816 for Rainfall Rates and Climate Change. *Climatic Change*, **39** (4), 667–694, doi:10.1023/A:
817 1005319109110.
- 818 Urey, H. C., 1947: The thermodynamic properties of isotopic substances. *J. Chem. Soc. (Resumed)*,
819 **0**, 562–581, doi:10.1039/JR9470000562.
- 820 Wallace, J. M., and P. V. Hobbs, 2006: *Atmospheric Science: An Introductory Survey*. Academic
821 Press, 483 pp.

822 Werner, M., M. Heimann, and G. Hoffman, 2001: Isotopic composition and origin of polar
823 precipitation in present and glacial climate simulations. *Tellus B*, **53** (1), 53–71, doi:10.1034/j.
824 1600-0889.2001.01154.x.

825 Werner, M., U. Mikolajewicz, M. Heimann, and G. Hoffmann, 2000: Borehole versus isotope
826 temperatures on Greenland: Seasonality does matter. *Geophys. Res. Lett.*, **27** (5), 723–726,
827 doi:10.1029/1999GL006075.

828 **LIST OF TABLES**

829 **Table A1.** Estimates of the temporal regression slope between the $\delta^{18}\text{O}$ of snow and local
830 surface temperature ($d\delta_p/dT_s$) based on analyses of ice cores in Greenland
831 (top) and Antarctica (bottom) spanning the LGM-Holocene deglaciation. The
832 first column gives the temporal slope (in ‰ K⁻¹), followed by the name and
833 coordinates of the ice core, the analysis method, and the source. Further details
834 are given in Appendix A4. 42

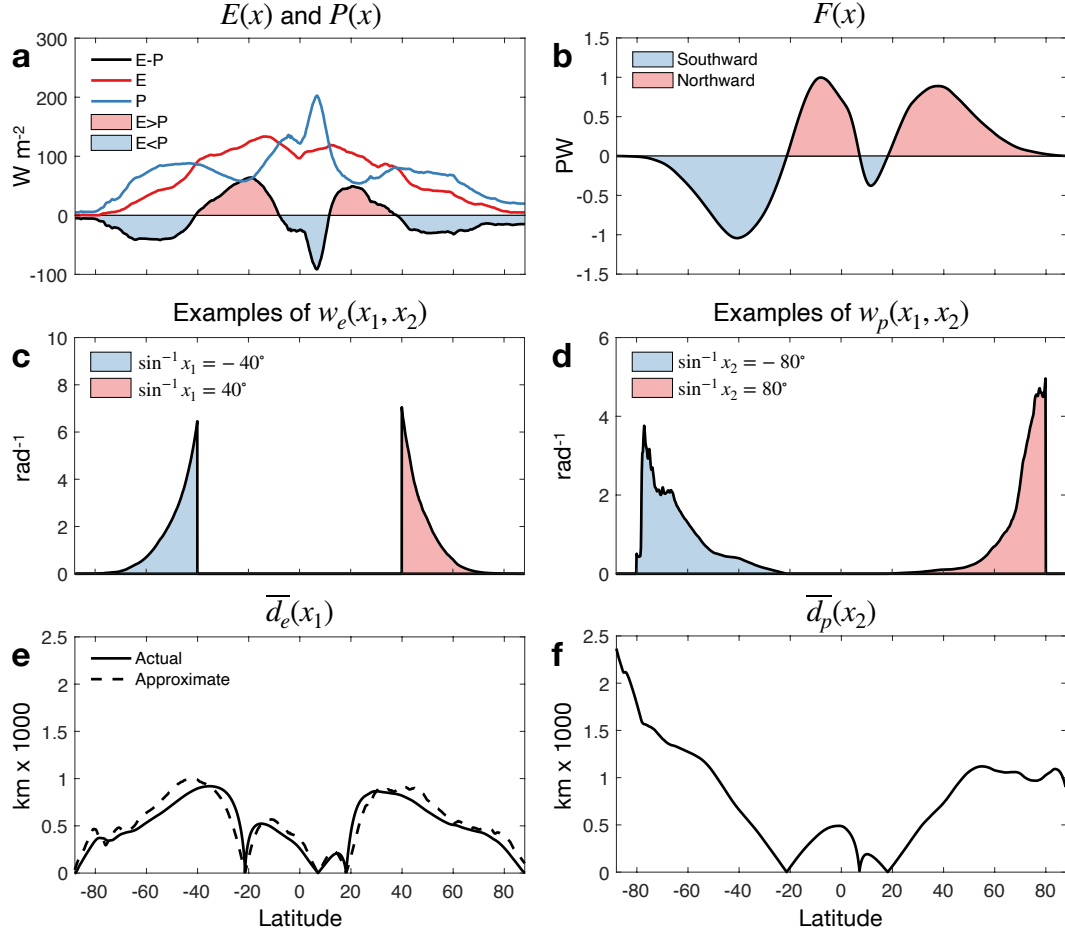
835 Table A1. Estimates of the temporal regression slope between the $\delta^{18}\text{O}$ of snow and local surface temperature
836 ($d\delta_p/dT_s$) based on analyses of ice cores in Greenland (top) and Antarctica (bottom) spanning the LGM-Holocene
837 deglaciation. The first column gives the temporal slope (in ‰ K^{-1}), followed by the name and coordinates of the
838 ice core, the analysis method, and the source. Further details are given in Appendix A4.

$d\delta_p/dT_s$	Site	Longitude	Latitude	Method	Source
GREENLAND					
0.33	GISP2	-38.48	72.58	Borehole	Cuffey et al. (1995)
0.30	GISP2	-38.48	72.58	$\delta^{15}\text{N}$	Buizert et al. (2014)
0.33	GRIP	-37.64	72.58	Borehole	Johnsen et al. (1995)
0.38	NGRIP	-42.32	75.10	$\delta^{15}\text{N}$	Kindler et al. (2014)
0.38	NGRIP	-42.32	75.10	$\delta^{15}\text{N}$	Buizert et al. (2014)
0.44	NEEM	-51.06	77.45	$\delta^{15}\text{N}$	Buizert et al. (2014)
ANTARCTICA					
0.88	Talos Dome	159.18	-72.82	Firn reconstruction	Buizert et al. (2021)
1.40	EDML	0	-75	Firn reconstruction	Buizert et al. (2021)
1.14	Dome C	123.3	-75.1	Borehole	Buizert et al. (2021)
1.45	EDC	123.3	-75.1	Firn reconstruction	Buizert et al. (2021)
1.44	Dome F	39.42	-77.19	Firn reconstruction	Buizert et al. (2021)
0.77	Vostok	106.80	-78.47	Borehole	Salamatin et al. (1998)
0.88	WAIS Divide	-112.10	-79.48	Borehole	Cuffey et al. (2016)
0.82	WAIS Divide	-112.10	-79.48	Firn reconstruction	Buizert et al. (2021)
0.80	Siple Dome	-148.81	-81.65	Firn reconstruction	Buizert et al. (2021)
1.19	South Pole	0	-90	Firn reconstruction	Buizert et al. (2021)

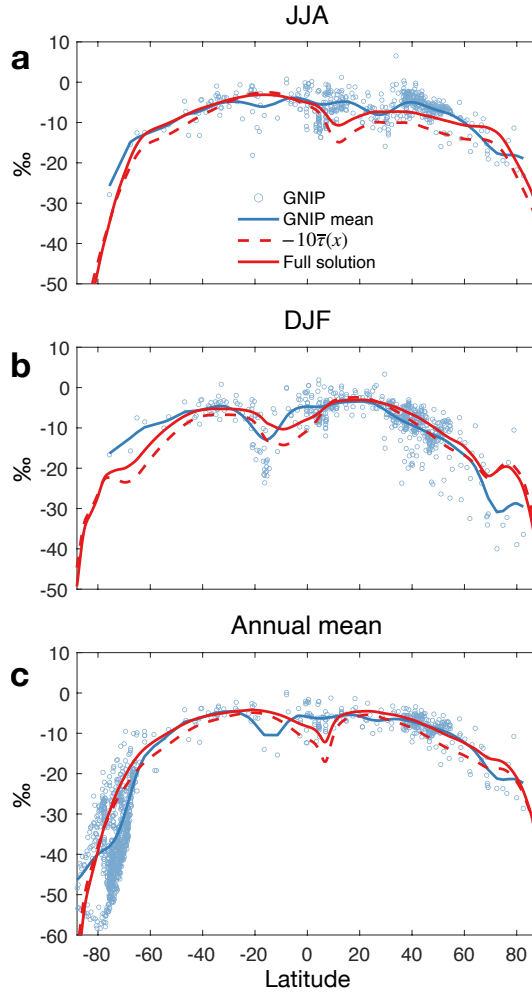
839

LIST OF FIGURES

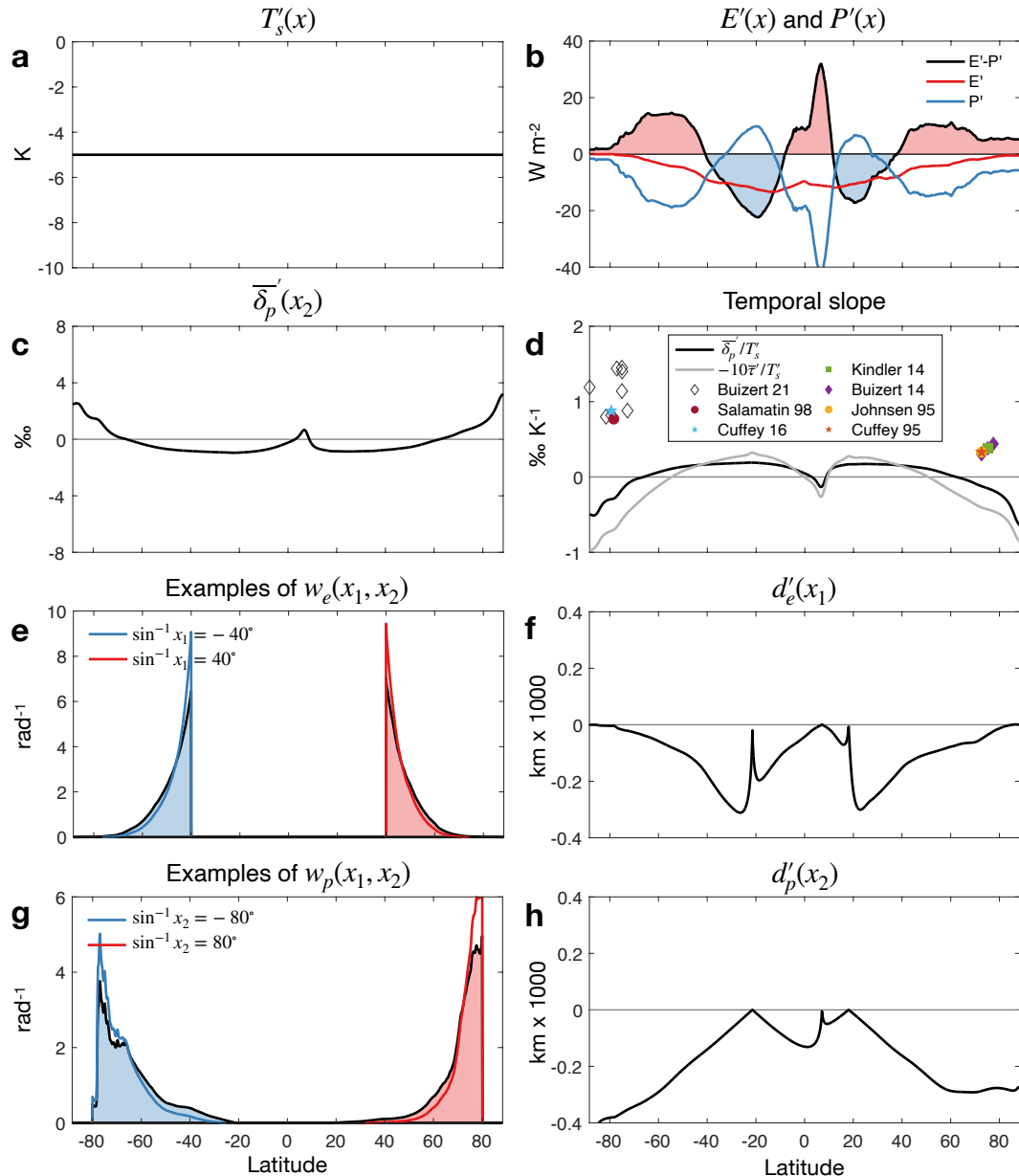
840		
841	Fig. 1.	(a) Zonal-mean, annual-mean E (red), P (blue), and $E - P$ (black) in the modern climate
842		(1979-2018), from ERA5 reanalysis. Red (blue) shading indicates latitudes where $E > P$
843		($E < P$). (b) Zonal-mean, annual-mean net northward atmospheric latent heat flux. Blue (red)
844		shading indicates net southward (northward) transport. (c) $w_e(x_1, x_2)$ at representative source
845		latitudes of -40° (blue) and 40° (red), representing the spatial distribution of precipitation
846		that results from evaporation at these latitudes. To convert from units of x^{-1} to θ^{-1} , we
847		multiply by $dx/d\theta = \cos \theta$. (d) $w_p(x_1, x_2)$ at representative sink latitudes of -80° (blue) and
848		80° (red), representing the spatial distribution of evaporation that contributes to precipitation
849		at these latitudes (in units of θ^{-1}). (e) The average distance vapor travels from each source
850		latitude, from Eq. 9 (solid line) and Eq. 10 (dashed line). (f) The average distance vapor
851		travels to each sink latitude from Eq. 11. 44
852	Fig. 2.	Average $\delta^{18}\text{O}$ of precipitation in (a) June-August, (b) December-February, and (c) the annual
853		mean. Blue dots indicate observations from the International Atomic Energy Agency/Global
854		Network of Isotopes in Precipitation (GNIP) data set. Seasonal data come from rain gauges,
855		while annual data come from rain gauges and Antarctic snow. Blue lines show the zonal-
856		mean of observations, computed using a moving Gaussian filter with $\sigma = 4^\circ$ latitude. The
857		dashed red line shows the approximation of $\overline{\delta_p}$ assuming constant fractionation of 10 ‰ (Eq.
858		17), computed using seasonal or annual means of $E(x)$ and $P(x)$ from ERA5. The solid
859		line shows the full solution for $\overline{\delta_p}$ that accounts for the influence of temperature and kinetic
860		effects on fractionation. 45
861	Fig. 3.	Scenario 1: uniform global cooling. (a) Change in zonal-mean T_s . (b) Changes in zonal-mean
862		E (red), P (blue), and $E - P$ (black). (c) Change in $\overline{\delta_p}$. (d) The temporal slope (black line),
863		approximated as the ratio of $\overline{\delta_p}'$ in (c) to T_s' in (a). The gray line shows the temporal slope
864		assuming constant fractionation of 10 ‰. Colored symbols represent independent estimates
865		of the temporal slope from polar ice cores (Table A1 and Appendix A4). (e) $w_e(x_1, x_2)$ at
866		the same latitudes as in Fig. 1c. Shading represents the modern climate, while colored lines
867		represent the cooler climate. (f) Change in the average distance vapor travels from each
868		source latitude. (g) $w_p(x_1, x_2)$ at the same latitudes as in Fig. 1d. Shading represents the
869		modern climate, while colored lines represent the cooler climate. (h) Change in the average
870		distance vapor travels to each sink latitude. 46
871	Fig. 4.	As in Fig. 3, but for Scenario 2: polar amplification. 47
872	Fig. 5.	As in Fig. 3, but for Scenario 3: temperature-dependent evaporation sensitivity. 48
873	Fig. 6.	(a) Zonal-mean T_s in the modern climate (blue) and the fractional change in zonal-mean E
874		per degree of zonal-mean warming (red; E'/ET_s') given by Eq. 25 with $G' = 0$. The dashed
875		red line shows a hemispherically-symmetric pattern of E'/ET_s' , representing the average of
876		the two hemispheres. (b) As in Fig. 5d, but with E' computed using the hemispherically-
877		symmetric scaling represented by the dashed line in (a). 49
878	Fig. 7.	(a) Change in zonal-mean T_s simulated by the MEBM with a uniform radiative forcing of -5
879		Wm^{-2} and feedback patterns diagnosed from 20 CMIP5 models. The yellow line represents
880		the ensemble mean. The other lines represent individual models, with deep blue indicating
881		much more cooling in the Northern Hemisphere, and deep red indicating roughly equal
882		cooling in both hemispheres. (b) The temporal slope ($\overline{\delta_p}'/T_s'$) computed using the HS06
883		approximation for E' , as in Scenario 2. (c) The temporal slope computed using the Penman
884		approximation for E' , as in Scenario 3. 50



885 FIG. 1. (a) Zonal-mean, annual-mean E (red), P (blue), and $E - P$ (black) in the modern climate (1979-
 886 2018), from ERA5 reanalysis. Red (blue) shading indicates latitudes where $E > P$ ($E < P$). (b) Zonal-mean,
 887 annual-mean net northward atmospheric latent heat flux. Blue (red) shading indicates net southward (northward)
 888 transport. (c) $w_e(x_1, x_2)$ at representative source latitudes of -40° (blue) and 40° (red), representing the spatial
 889 distribution of precipitation that results from evaporation at these latitudes. To convert from units of x^{-1} to
 890 θ^{-1} , we multiply by $dx/d\theta = \cos \theta$. (d) $w_p(x_1, x_2)$ at representative sink latitudes of -80° (blue) and 80° (red),
 891 representing the spatial distribution of evaporation that contributes to precipitation at these latitudes (in units of
 892 θ^{-1}). (e) The average distance vapor travels from each source latitude, from Eq. 9 (solid line) and Eq. 10 (dashed
 893 line). (f) The average distance vapor travels to each sink latitude from Eq. 11.



894 FIG. 2. Average $\delta^{18}\text{O}$ of precipitation in (a) June-August, (b) December-February, and (c) the annual mean.
 895 Blue dots indicate observations from the International Atomic Energy Agency/Global Network of Isotopes in
 896 Precipitation (GNIP) data set. Seasonal data come from rain gauges, while annual data come from rain gauges
 897 and Antarctic snow. Blue lines show the zonal-mean of observations, computed using a moving Gaussian filter
 898 with $\sigma = 4^\circ$ latitude. The dashed red line shows the approximation of $\overline{\delta_p}$ assuming constant fractionation of 10
 899 ‰ (Eq. 17), computed using seasonal or annual means of $E(x)$ and $P(x)$ from ERA5. The solid line shows the
 900 full solution for $\overline{\delta_p}$ that accounts for the influence of temperature and kinetic effects on fractionation.



901 FIG. 3. Scenario 1: uniform global cooling. (a) Change in zonal-mean T_s . (b) Changes in zonal-mean E (red),
 902 P (blue), and $E - P$ (black). (c) Change in $\overline{\delta_p'}$. (d) The temporal slope (black line), approximated as the ratio of
 903 $\overline{\delta_p'}$ in (c) to T_s' in (a). The gray line shows the temporal slope assuming constant fractionation of 10 ‰. Colored
 904 symbols represent independent estimates of the temporal slope from polar ice cores (Table A1 and Appendix
 905 A4). (e) $w_e(x_1, x_2)$ at the same latitudes as in Fig. 1c. Shading represents the modern climate, while colored
 906 lines represent the cooler climate. (f) Change in the average distance vapor travels from each source latitude.
 907 (g) $w_p(x_1, x_2)$ at the same latitudes as in Fig. 1d. Shading represents the modern climate, while colored lines
 908 represent the cooler climate. (h) Change in the average distance vapor travels to each sink latitude.

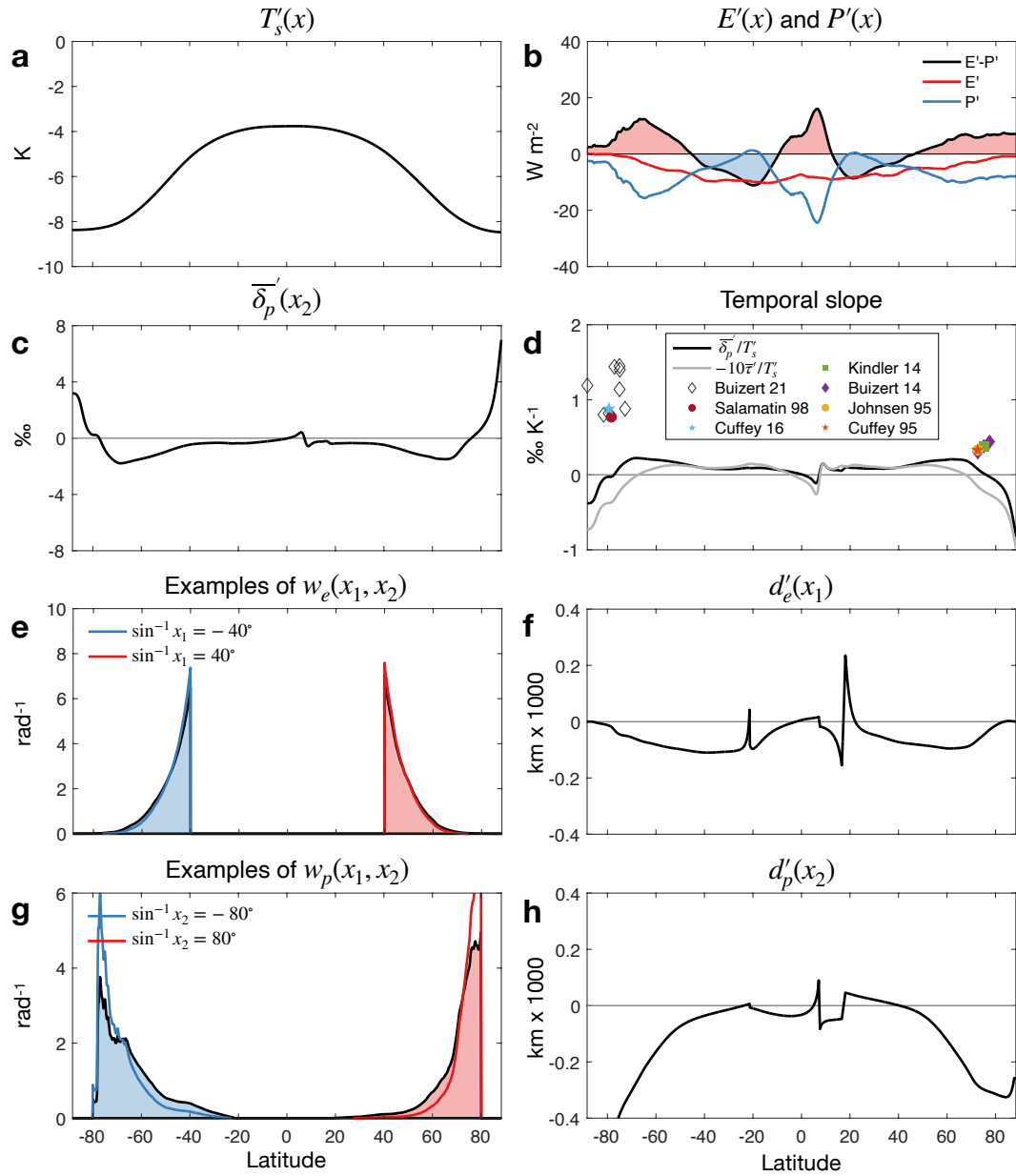


FIG. 4. As in Fig. 3, but for Scenario 2: polar amplification.

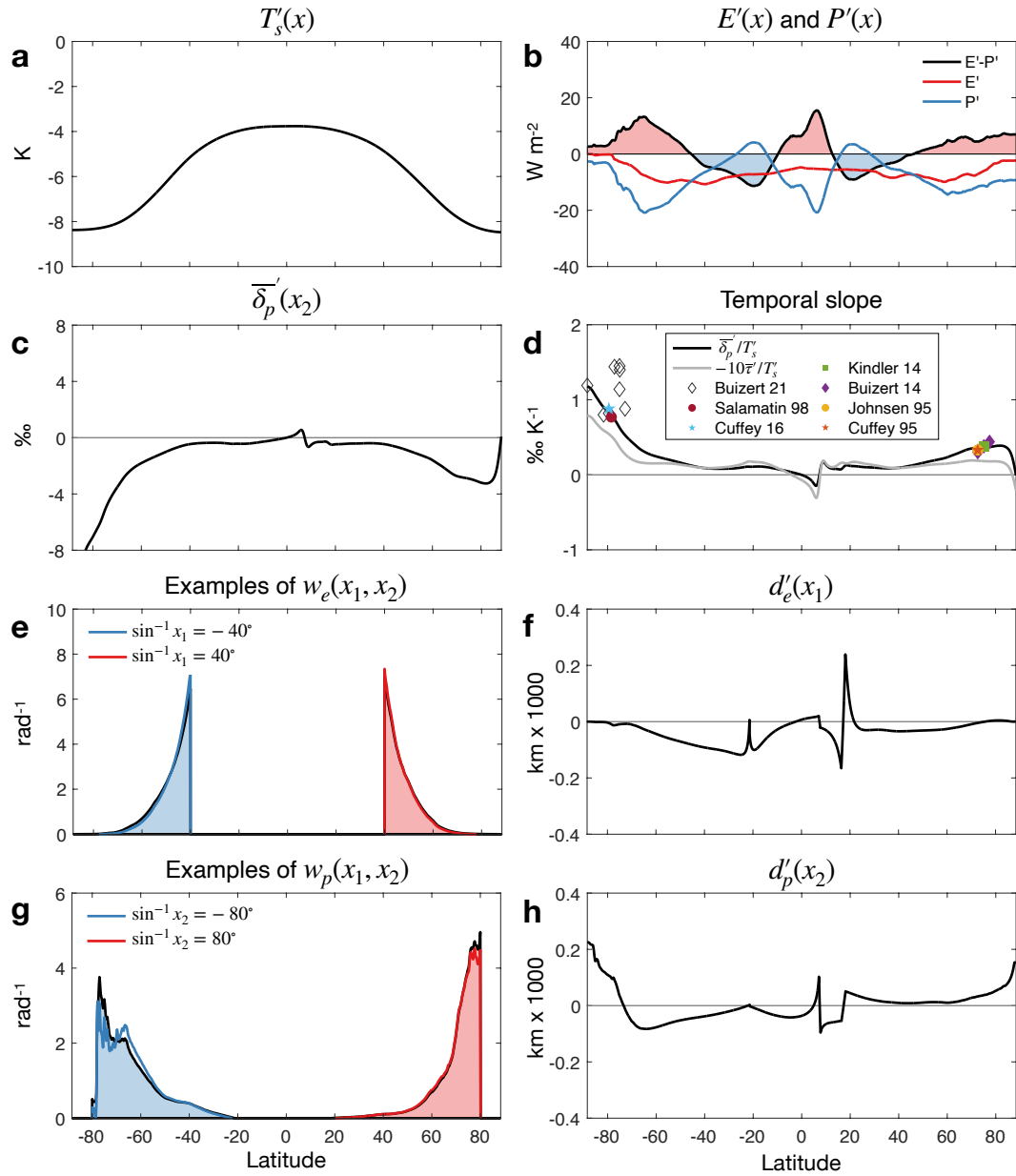
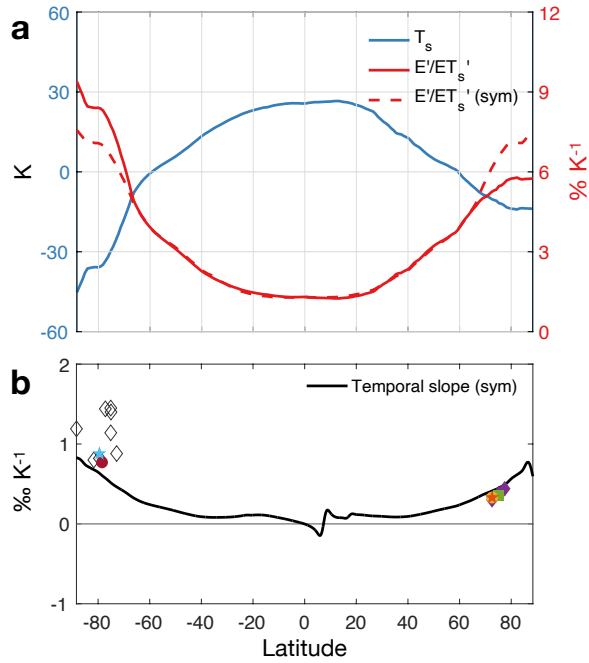
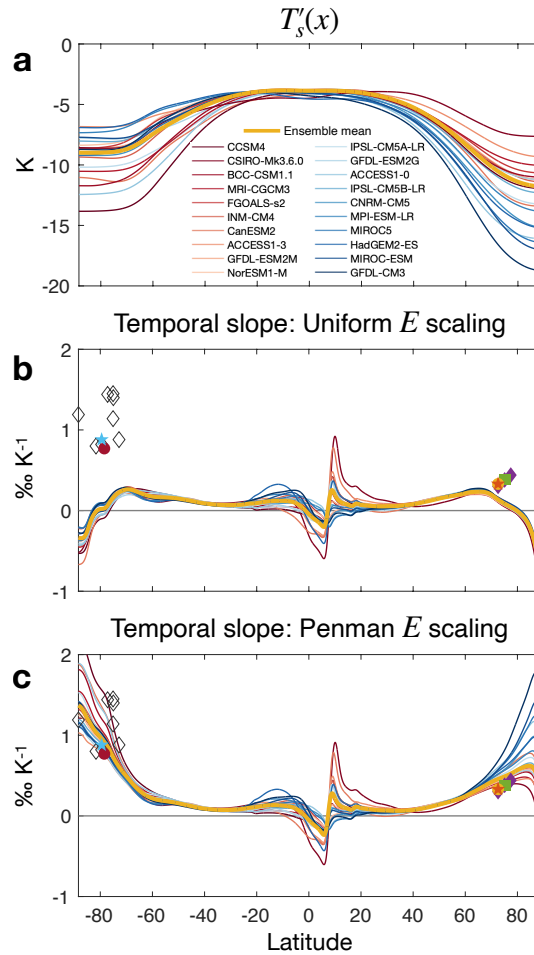


FIG. 5. As in Fig. 3, but for Scenario 3: temperature-dependent evaporation sensitivity.



909 FIG. 6. (a) Zonal-mean T_s in the modern climate (blue) and the fractional change in zonal-mean E per degree of
 910 zonal-mean warming (red; E'/ET'_s) given by Eq. 25 with $G' = 0$. The dashed red line shows a hemispherically-
 911 symmetric pattern of E'/ET'_s , representing the average of the two hemispheres. (b) As in Fig. 5d, but with E'
 912 computed using the hemispherically-symmetric scaling represented by the dashed line in (a).



913 FIG. 7. (a) Change in zonal-mean T_s simulated by the MEBM with a uniform radiative forcing of -5 Wm^{-2} and
 914 feedback patterns diagnosed from 20 CMIP5 models. The yellow line represents the ensemble mean. The other
 915 lines represent individual models, with deep blue indicating much more cooling in the Northern Hemisphere,
 916 and deep red indicating roughly equal cooling in both hemispheres. (b) The temporal slope ($\overline{\delta_p}'/T'_s$) computed
 917 using the HS06 approximation for E' , as in Scenario 2. (c) The temporal slope computed using the Penman
 918 approximation for E' , as in Scenario 3.



Click here to access/download

Supplemental Material

Isotopes_JC_supplemental_R2.pdf

